Human organotypic colon in vitro microtissue: unveiling a new window into colonic drug disposition

Pedro G.M. Canhão , Jan Snoeys , Suzy Geerinckx , Marjolein van Heerden , An Van den Bergh , Camden Holm , Jan Markus , Seyoum Ayehunie , Mario Monshouwer , Raymond Evers , Patrick Augustijns , Stephanie Kourula

PII: S0928-0987(25)00024-7
DOI: https://doi.org/10.1016/j.ejps.2025.107025
Reference: PHASCI 107025

To appear in: *European Journal of Pharmaceutical Sciences*

Received date: 6 December 2024
Revised date: 22 January 2025
Accepted date: 23 January 2025

Please cite this article as: Pedro G.M. Canhão , Jan Snoeys , Suzy Geerinckx , Marjolein van Heerden , An Van den Bergh , Camden Holm , Jan Markus , Seyoum Ayehunie , Mario Monshouwer , Raymond Evers , Patrick Augustijns , Stephanie Kourula , Human organotypic colon in vitro microtissue: unveiling a new window into colonic drug disposition, *European Journal of Pharmaceutical Sciences* (2025), doi: https://doi.org/10.1016/j.ejps.2025.107025

To be submitted to the *European Journal of Pharmaceutical Sciences*

Highlights

- EpiColon mimics structural and cellular features of the human colon.
- EpiColon demonstrates TEER comparable to native human colonic tissue.
- EpiColon discriminates between high and low permeable drugs.
- EpiColon may help rank small molecules in the low permeability category.
- EpiColon exhibits incomplete epithelial maturation with flat and cuboidal cells.

Human organotypic colon *in vitro* microtissue: unveiling a new window into colonic drug disposition

Author names

Pedro G.M. Canhão [a,c], Jan Snoeys [a], Suzy Geerinckx [a], Marjolein van Heerden [a], An Van den Bergh [a], Camden Holm [d], Jan Markus [e], Seyoum Ayehunie [d], Mario Monshouwer [a], Raymond Evers [b], Patrick Augustijns [c] and Stephanie Kourula [a,*]

Affiliations

[a] *Preclinical Sciences & Translational Safety, Janssen R&D, Turnhoutseweg 30, 2340, Beerse, Belgium*

[b] *Preclinical Sciences & Translational Safety, Janssen R&D, LLC, Spring House, Pennsylvania, USA*

[c] *Drug Delivery and Disposition, KU Leuven, Gasthuisberg O&N II, Herestraat 49 – box 921, 3000 Leuven, Belgium*

[d] *MatTek Corporation, 200 Homer Avenue, Ashland, Massachusetts, USA*

[e] *MatTek In Vitro Life Science Laboratories, Bratislava, Slovak Republic*

Corresponding authors

***** Corresponding author at: Preclinical Sciences & Translational Safety, Janssen R&D, Turnhoutseweg 30, 2340, Beerse, Belgium.

E-mail address: skourula@its.jnj.com (S. Kourula).

Number of main figures: 5 (Figs. 1–5)
Number of main tables: 1 (Table 1)
Number of supplementary figures (appendix A): 8 (Figs. S1–8)
Number of supplementary tables (appendix B): 10 (Tables S1–10)

Abbreviations

ALI, Air-liquid interface; **BCRP**, Breast cancer resistance protein; **BCS**, Biopharmaceutics classification system; **CR**, Controlled release; **CRC**, Colorectal cancer; **DME**, Drug metabolizing enzyme; **DMEM**, Dulbecco's modified Eagle's medium; **DPBS**, Dulbecco's phosphate-buffered saline; **DT**, Drug transporter; f_{abs}, Fraction absorbed compound; **FITC**, Fluorescein isothiocyanate; **GI**, Gastrointestinal; **H&E**, Hematoxylin and eosin; **IBD**, Inflammatory bowel disease; **i.c.**, Intracolonic administration; **IR**, Immediate release; **IVIVCs**, In vitro-in vivo correlations; **Ki-67**, Marker of proliferation Kiel 67; **LC**, Liquid chromatography; **MEM NEAA**, Minimum essential medium non-essential amino acids; **MRP2**, Multidrug resistance protein 2; **MS**, Mass spectrometry; **PanCK**, Pan-Cytokeratin; P_{app}, Apparent permeability coefficient; **P-gp**, P-glycoprotein; **p.o.**, Per oral administration; R^2, Square of the Pearson correlation coefficient *r* or coefficient of determination; r_s, Spearman's rank correlation coefficient; **SI**, Small intestine; **TEER**, Transepithelial electrical resistance; **UHPLC**, Ultra high-performance liquid chromatography.

To be submitted to the *European Journal of Pharmaceutical Sciences*

Graphical Abstract

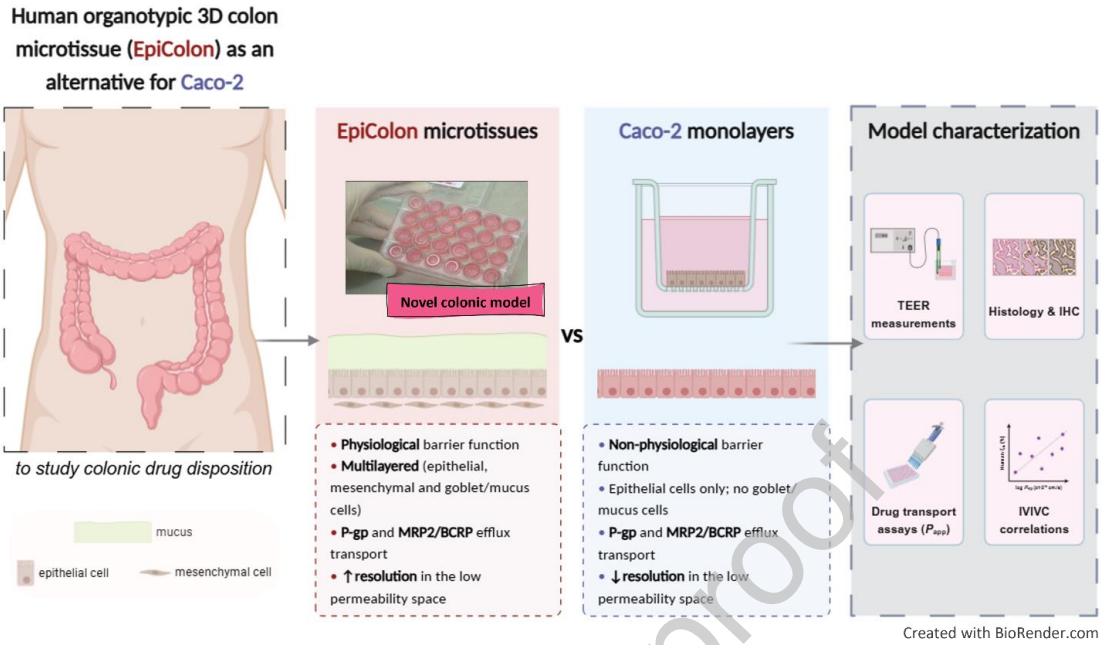

Abstract

The purpose of this study was to evaluate EpiColon, a novel human organotypic 3D colon microtissue prototype, developed to assess colonic drug disposition, with a particular focus on permeability ranking, and compare its performance to Caco-2 monolayers.

EpiColon was characterized for barrier function using transepithelial electrical resistance (TEER), morphology via histology and immunohistochemistry, and functionality through drug transport studies measuring apparent permeability (P_{app}). Cutoff thresholds for the permeability of FITC–dextran 4 kDa (FD4), FITC–dextran 10 kDa (FD10S), and [^{14}C]mannitol were established to monitor microtissue integrity. Permeability of EpiColon for 20 benchmark drugs was compared with Caco-2 data, and the activity of pivotal efflux transporters, including multidrug resistance protein 1/P-glycoprotein (MDR1/P-gp), along with multidrug resistance protein 2 (MRP2) and breast cancer resistance protein (BCRP), was evaluated using selective substrates.

EpiColon exhibited a physiological barrier function (272.0 ± 53.05 Ω x cm^2) and effectively discriminated between high (e.g., budesonide and [^{3}H]metoprolol) and low permeable compounds (e.g., [^{3}H]atenolol and [^{14}C]mannitol). The model demonstrated functional activity for key efflux transporters, with efflux ratios of 2.32 for [^{3}H]digoxin (MDR1/P-gp) and 3.34 for sulfasalazine (MRP2 and BCRP). Notably, EpiColon showed an enhanced dynamic range in the low permeability range, differentiating P_{app} between FD4 and FD10S, in contrast to Caco-2 monolayers. Significant positive correlations were observed between human fraction absorbed (f_{abs}) and logarithmically transformed P_{app} [AP-BL] values for both EpiColon (r_s = 0.68) and Caco-2 (r_s = 0.68). Furthermore, EpiColon recapitulates some essential phenotypic and cellular features of the human colon, including the expression of critical marker genes (Pan-Cytokeratin$^+$: epithelial/colonocytes, Vimentin$^+$: mesenchymal/fibroblast, and Alcian Blue$^+$: goblet cell/mucus).

In conclusion, EpiColon is a promising platform that offers a valuable complement to conventional Caco-2 monolayers for studying colonic drug disposition. However, the presence of flat and some cuboidal cells, along with low throughput, must be addressed to improve its applicability in both academic research and pharmaceutical industry.

Keywords: Drug absorption; Drug disposition; Intestinal *in vitro* tools; Intestinal permeability; Organotypic colon microtissues; Pharmacokinetics.

1. Introduction

The oral route remains the most preferred method for drug delivery due to its non-invasive nature and suitability for self-administration (Dahlgren et al., 2015; Hua, 2020; Macedo et al., 2020). It is effective for both systemic drug delivery and for targeting local gastrointestinal (GI) diseases (Hua, 2020; Lemmens et al., 2021). However, poor drug stability, limited solubility, and low permeation across mucosal barriers are significant factors contributing to the attrition of oral drug candidates (Koziolek et al., 2023).

More than 60% of marketed drugs are orally administered, with about 90% absorbed in the small intestine (SI) (Pretorius and Bouic, 2009). Consequently, the colon typically plays a secondary role in systemic drug absorption, as most drugs are absorbed in the SI before reaching the colon (Vinarov et al., 2021). Although the colon differs structurally and functionally from the SI, it is particularly well-suited for controlled release (CR) formulations (Tannergren et al., 2009; Vinarov et al., 2021), due to its longer transit time (often exceeding 24 hours, compared to 2–5 hours in the SI) (Ehrhardt and Kim, 2008; Tannergren et al., 2009). In addition, oral CR products may offer several advantages *vis-à-vis* their immediate release (IR) counterparts, including extended exposure, prolonged effect duration, reduced side effects, and improved patient compliance (Koziolek et al., 2023; Tannergren et al., 2009). Extended exposure resulting from an oral CR strategy is also advantageous for drugs with low water solubility, which limits their dissolution rate and, consequently, their bioavailability (Peña, 2022).

Colonic drug delivery is crucial for treatment of local diseases, such as colorectal cancer (CRC) and inflammatory bowel disease (IBD). CRC ranks as the third most common cancer and the second leading cause of cancer-related deaths worldwide (Marcellinaro et al., 2024). IBD, encompassing Crohn's disease (CD) and ulcerative colitis (UC), affects over 0.3% of the global population, posing a significant public health challenge (Hammer and Langholz, 2020; Xu et al., 2024). Both CRC and IBD impose a substantial burden on patients and healthcare systems (Kaplan, 2015; Marr et al., 2023; Panaccione et al., 2005). Effective treatment of these conditions hinges on achieving sufficient drug penetration and accumulation within the colonic epithelium, ensuring higher concentrations in diseased tissues while minimizing systemic exposure. Local drug delivery enables enhanced colonic exposure, thereby maximizing therapeutic efficacy and minimizing unwanted systemic side effects (Steigert et al., 2024; Tannergren et al., 2009).

Current *in vitro* models of the intestine mainly focus on the upper GI tract, lacking the capacity to accurately emulate absorption and metabolism in the colon (Madden et al., 2018; Yoshida et al., 2021). Moreover, these models frequently display weak in vitro-in vivo correlations (IVIVCs) for poorly permeable molecules like macrocycles, other beyond Rule of 5 (bRo5) compounds, and peptides, resulting in

suboptimal local drug delivery strategies (Koziolek et al., 2023; Larregieu and Benet, 2014; Vinarov et al., 2021).

Conventional *in vitro* cell lines, such as the human colorectal adenocarcinoma-derived Caco-2 (Hubatsch et al., 2007) and Madin-Darby canine kidney (MDCK) cells (Di et al., 2020), along with *ex vivo* intestinal models like rodent explants (e.g., Ussing chambers) (Roos et al., 2017), exhibit considerable limitations. These models often fail to replicate human physiology due to their cancerous origin or interspecies differences (Yoshida et al., 2021; Zachos et al., 2016). Human intestinal Ussing chambers, while closely mimicking human intestinal physiology and predicting the human fraction absorbed (f_{abs}) (Sjöberg et al., 2013), are technically demanding, time-consuming, and not easily scalable due to limited tissue availability and short tissue viability (Michiba et al., 2022; Rozehnal et al., 2012; Sjöberg et al., 2013; Streekstra et al., 2022).

Caco-2 monolayers, despite being considered the gold standard for drug absorption studies and retaining many morphological and functional properties of enterocytes (Costa and Ahluwalia, 2019; Hubatsch et al., 2007; Kus et al., 2023; Larregieu and Benet, 2013), form non-physiological monolayers with significantly tighter, less permeable paracellular junctions than the native human intestinal epithelium (Ayehunie et al., 2018). They also show altered expression levels of drug metabolizing enzymes (DMEs) and drug transporters (DTs) (Englund et al., 2006; Lu et al., 2022; Müller et al., 2017; Ölander et al., 2016), lack mucus-producing cells (Ayehunie et al., 2018; Kwon et al., 2021), and present very low cytochrome P450 (CYP)3A activity (Ayehunie et al., 2018; Cui et al., 2020), along with morphological and functional variability due to passage number and heterogeneity between subclones (Ayehunie et al., 2018; Kus et al., 2023). The transepithelial electrical resistance (TEER) of Caco-2 monolayers (195 to 2400 Ω x cm^2) also differs markedly from human small intestinal (12 to 120 Ω x cm^2) and human colonic tissues (300 to 400 Ω x cm^2) (Ayehunie et al., 2018; Darling et al., 2020; Hubatsch et al., 2007; Srinivasan et al., 2015). However, when conducting drug transport studies, TEER values near 2000 Ω x cm^2, indicative of a tight epithelium, should be carefully considered, as they may not be suitable for such investigations. GI epithelia are categorized based on TEER values, with "tight" epithelia exhibiting resistance around 2000 Ω x cm^2 and "leaky" epithelia displaying values between 50 and 100 Ω x cm^2 (Srinivasan et al., 2015).

In 2011, Sato et al. developed a method to isolate stem cells from the human intestine and grow them into three-dimensional (3D) structures called human intestinal organoids (HIOs) (Sato et al., 2011). Unlike Caco-2 cells, these organoids resemble epithelial physiology in a region-specific manner (Kraiczy et al., 2019) and retain donor phenotypes for up to 17 passages (van der Hee et al., 2020). They are also easy to handle, compatible with long-term culture and expansion, and amenable to cryopreservation (d'Aldebert et al., 2020; In et al., 2019; Mahe et al., 2015; Sato et al., 2011, 2009; Wang et al., 2019; Zietek et al., 2020). Although promising, their 3D structure, with a closed lumen and inward-oriented epithelia, limits their utility in drug disposition studies due to restricted access to the apical surface (In et al., 2019; Kwon et al., 2021; VanDussen et al., 2015). This can be circumvented using alternative techniques, such as microinjection (Arian et al., 2024), membrane polarity flipping (Arian et al., 2024), or forming Transwell®-based 2D monolayers (Ambrosini et al., 2020; In et al., 2019; Kwon et al., 2021; VanDussen et al., 2015), which allows access to both apical and basal surfaces (Arian et al., 2024; Kourula et al., 2023).

Emerging evidence suggests that more physiologically relevant *in vitro* systems, like human GI microtissues, enable better predictions of oral drug absorption than Caco-2 monolayers (Ayehunie et al.,

2018). The EpiIntestinal™ microtissue, derived from a 19-year-old female donor's ileum, has been validated for assessing intestinal drug disposition (Cui et al., 2020; Markus et al., 2021) and safety (Peters et al., 2019). These GI microtissues provide direct access to both basal and apical surfaces, with key advantages, including the use of primary cells, tissue polarization, and the expression of DMEs and DTs akin to native tissue (Ayehunie et al., 2018; Cui et al., 2020; Peters et al., 2019).

Given the limitations of existing *in vitro* systems, more complex, translatable, and *in vivo*-relevant colonic models with enhanced cellular diversity and function are needed. This study aims to comprehensively characterize a novel organotypic 3D colon microtissue prototype (*EpiColon*) as a platform for investigating colonic drug disposition, complementing the widely used Caco-2 monolayers. We focus on evaluating the barrier function, structural features, activity of relevant DTs such as MDR1/P-glycoprotein (P-gp), along with multidrug resistance protein 2 (MRP2) and breast cancer resistance protein (BCRP), and the permeability of the microtissue for 20 model drugs, comparing these findings with data obtained with Caco-2 monolayers.

2. Materials and methods

2.1. Chemicals and reagents

Antipyrine, budesonide, ketoprofen, sumatriptan, mesalazine, ximelagatran, sulfasalazine, ranitidine, erythromycin, fluorescein isothiocyanate (FITC)–dextran 4 kDa (FD4), fluorescein isothiocyanate (FITC)–dextran 10 kDa (FD10S), elacridar (GF120198), MK571 sodium salt hydrate, and tolbutamide were obtained from Sigma-Aldrich (Overijse, Belgium). Celecoxib, sulindac, and cyclosporin A (CsA) were provided by Johnson & Johnson Innovative Medicine (Beerse, Belgium), while inogatran was supplied by Johnson & Johnson Innovative Medicine (Spring House, PA, USA). [^{3}H]metoprolol and [^{3}H]atenolol were sourced from Moravek, Inc. (Brea, CA, USA). [^{3}H]digoxin and [^{14}C]mannitol were acquired from PerkinElmer (Waltham, MA, USA), and [^{14}C]cimetidine from American Radiolabeled Chemicals, Inc. (Saint Louis, MO, USA). Ultima Gold™ Liquid Scintillation Cocktail was procured from Revvity Health Sciences, Inc. (Waltham, MA, USA).

Dimethyl sulfoxide (DMSO), methanol, formic acid, and the ultrapure water system Milli-Q® IQ 7000 with Millipak® 0.22 µm hydrophilic membrane filter were purchased from Merck KGaA (Darmstadt, Germany). Acetonitrile was sourced from Biosolve Chimie (Dieuze, France) and ammonium formate from VWR Chemicals (Amsterdam, The Netherlands). All solvents were of analytical grade.

Dulbecco's phosphate-buffered saline with Ca^{2+} and Mg^{2+} ($DPBS^{++}$), Dulbecco's phosphate-buffered saline without Ca^{2+} and Mg^{2} (DPBS), Hanks' balanced salt solution (HBSS), Dulbecco's modified Eagle's medium (DMEM), minimum essential medium non-essential amino acids (MEM NEAA), fetal bovine serum (FBS), penicillin/streptomycin (Pen/Strep), and L-glutamine were all obtained from Thermo Fisher Scientific (Gibco™; Merelbeke, Belgium). D-(+)-glucose and 4-(2-hydroxyethyl)-1-piperazineethanesulfonic acid (HEPES) were sourced from Sigma-Aldrich (Overijse, Belgium).

All other reagents utilized in the methods described are detailed in their respective sections below.

2.2. In vitro systems

2.2.1. Human 3D colon microtissue culture

Primary human colon epithelial cells, sourced from the descending colon of a single donor, were purchased from a commercial vendor, complying with all applicable local, state, and federal laws and regulations. These cells were expanded at MatTek Corporation (Ashland, MA, USA) using a modified cell expansion medium, which was refreshed 3 times per week.

For microtissue reconstruction, cryopreserved cells were thawed, plated in Nunc™ EasYFlask™ T-75 cell culture flasks (Thermo Fisher Scientific, Waltham, MA, USA), and cultured in a proprietary expansion medium (MatTek Corporation). After expansion, cells were trypsinized, counted and seeded at a density of 3.0 x 10^5 cells/cm^2 onto collagen-coated cell culture inserts (MatTek Corporation, 0.6 cm^2). The cells were cultured for 3 days under submerged conditions before being transitioned to an air-liquid interface (ALI) in a proprietary differentiation medium (Col-100-MM, MatTek Corporation). During the ALI phase, the tissues were fed basolaterally through the membrane of the cell culture inserts and apically with minimal volume, with medium refreshment occurring 3 times per week.

Differentiation into colonocytes, goblet cells and mesenchymal cells was achieved over a period of 11 to 14 days (varying by tissue batch). This process resulted in the development of differentiated tissues, referred to as *EpiColon* or *Col-100*. Henceforth, the term *EpiColon* will specifically refer to the prototype version of these organotypic 3D colon microtissues in their differentiated state. Structural and functional evaluations were performed on three distinct batches of tissues after being shipped from MatTek Corporation to the Johnson & Johnson Innovative Medicine facilities (Beerse, Belgium).

2.2.2. Caco-2 monolayer culture

Caco-2 cells (ATCC, HTB-37™, lot number: 7001334) were obtained from the American Tissue Culture Collection (Rockville, MD, USA). For this study, cells within a low passage interval (19–23) were utilized. Following thawing, cells were plated in T-75 tissue culture flasks (VWR®, Radnor, PA, USA) and incubated at 37 °C, 5% CO_2 and 95% relative humidity. Cells were harvested with trypsin-EDTA, counted, and seeded at a density of 6.3 x 10^4 cells/cm^2 onto 24-well cell culture inserts (Millicell®-PCF, 0.4 µm, 12 mm Ø, 0.7 cm^2). The culture medium consisted of DMEM (Gibco™, #41965-039) supplemented with 20% FBS (Gibco™, #10270-106), 1% MEM NEAA (Gibco™, #11140-035), 1% L-glutamine (Gibco™, #25030-024) and 100 U/mL Pen/Strep (Gibco™, #15070-063) and was replaced one day after seeding and every 2 to 3 days thereafter. After 21 days of culture, the Caco-2 monolayers were used for the subsequent experiments.

2.3. Model characterization

2.3.1. Histology and Immunohistochemistry (IHC)

After 3 to 11 days of differentiation, colon microtissues were washed with DPBS and subsequently fixed at room temperature in 4% formalin (Sigma-Aldrich) for 30 min. Post-fixation, tissues were rehydrated through a series of ethanol washes, embedded in paraffin blocks, and sectioned at a thickness of 5 µm.

Hematoxylin and Eosin (H&E) staining was carried out automatically using the Ventana HE 600 Staining System (Roche Diagnostics).

For IHC, sections were processed on a Ventana Discovery Ultra Research Staining System (Roche Diagnostics) according to the manufacturer's protocols. In brief, the process involved deparaffinization,

Tris-EDTA-based antigen retrieval, quenching of endogenous peroxidases, and incubation with primary antibodies, including Pan-Cytokeratin (PanCK), Vimentin, and Marker of Proliferation Kiel 67 (Ki-67), followed by horseradish peroxidase (HRP)-conjugated secondary antibodies. Detailed information on these antibodies is provided in *Supplementary Table 1* (**Appendix B.1**, **Table S1**). Detection of positive signals was achieved using a 3,3'-diaminobenzidine (DAB) chromogenic detection kit, with Hematoxylin II and bluing reagent serving as counterstains. For Alcian Blue chemical staining, sections were deparaffinized, immersed in 3% acetic acid, stained with a 1% Alcian Blue solution, and counterstained with nuclear fast red. Scans were captured using the NanoZoomer-XR Automated slide scanner (Hamamatsu Photonics).

2.3.2. Protein determination

Total protein concentration was determined using the bicinchoninic acid (BCA) method with the Pierce™ BCA Protein Assay Kit (Thermo Fisher Scientific, #23227), according to the provider's protocol. Absorbance was measured at 562 nm with a Tecan Spark® 10M High Performance Multi-Mode Microplate Reader (Männedorf, Switzerland).

2.3.3. Drug transport studies

Human 3D colon microtissues were prepared as detailed in Section 2.2.1, transported to Johnson & Johnson Innovative Medicine facilities (Beerse, Belgium), and cultured until the endpoint of differentiation, typically between days 11 and 14, prior to dosing. Caco-2 monolayers were used at day 21.

Both microtissues and Caco-2 monolayers were washed twice with HBSS (containing Ca^{2+} and Mg^{2+}) supplemented with 10 mM HEPES (pH 7.4) on both apical and basolateral sides (transport medium). For microtissues, the transport medium was additionally supplemented with 11 mM D-(+)-glucose. Drug transport experiments were initiated by applying transport medium containing test drugs into the apical compartment, while the basolateral compartment received transport medium with 0.5% DMSO (400 µL apical and 800 µL basolateral in both systems). For drugs known to be substrates for specific transporters—such as cyclosporin A, erythromycin, and digoxin for P-gp, and sulfasalazine for MRP2 and BCRP—the transport medium containing test drugs was applied to either the apical or basolateral compartments, depending on the transport direction under investigation. These experiments were conducted both in the presence and absence of an inhibitor. Information on physicochemical properties, test drug and inhibitor concentrations (where applicable), sampling timepoints, transport directions and quantification methods is provided in *Supplementary Table 2* (**Appendix B.1**, **Table S2**). The *in vitro* systems were incubated at 37 °C in a humidified incubator with 5% CO_2. Each experimental condition was tested in triplicate, with transport measurements carried out in the apical-to-basolateral (AP→BL) direction for passively transported drugs, and in both the AP→BL and basolateral-to-apical (BL→AP) directions for transporter substrates, as specified in **Table S2**.

Prior to initiating the experiments, starting solutions of each test drug were sampled to verify their initial concentrations (C_{t0}). Subsamples were collected from both apical and basolateral sides at 30 and 60 min. At the end of the incubation period (120 min), samples were taken from both donor and receiver compartments to assess compound recovery. The concentrations of [^{3}H]atenolol, [^{3}H]metoprolol,

[^{3}H]digoxin, [^{14}C]cimetidine and [^{14}C]mannitol were determined by liquid scintillation counting (LSC). Radiolabeled samples were mixed with 4 mL of Ultima Gold™ liquid scintillation cocktail in liquid scintillation vials. Radioactivity was then measured with a Tri-Carb 4910TR liquid scintillation counter (PerkinElmer, Boston, MA, USA). Fluorescence detection of FD4 and FD10S was performed with a Tecan Spark® 10M High Performance Multi-Mode Microplate Reader (Männedorf, Switzerland) at excitation/emission wavelengths of 490/520 nm. All other compounds were analyzed by LC-MS/MS.

2.3.4. Quality control (QC) parameters

2.3.4.1. Transepithelial electrical resistance (TEER) measurements

TEER was employed as an initial control metric to evaluate tissue integrity within each insert of both EpiColon and Caco-2 models. TEER assessments were systematically conducted both before ($TEER_{pre\text{-}assay}$) and after ($TEER_{post\text{-}assay}$) the transport assays. These measurements were performed using an EVOM epithelial Voltohmmeter paired with an STX2 electrode set (World Precision Instruments), with all readings taken on a 37 °C heating plate.

TEER values, reported in Ω x cm^2, were calculated by subtracting the resistance of an empty insert from the recorded raw resistance measurements and subsequently multiplying the resulting value by the surface area of the respective tissue culture insert (0.6 cm^2 for EpiColon and 0.7 cm^2 for Caco-2).

For EpiColon, an integrity threshold of 100 Ω x cm^2 was established by MatTek Corporation. Only microtissues exhibiting TEER values ≥ 100 Ω x cm^2 were included in the study. Since EpiColon is a novel model, TEER was tightly monitored over time until the culture endpoints, across three distinct batches (*n* = 10–116 wells), to evaluate batch-to-batch tissue reproducibility. For Caco-2, TEER was measured on day 21, and only wells exhibiting TEER values ≥ 195 Ω x cm^2 were selected for further analyses (Hubatsch et al., 2007).

2.3.4.2. Paracellular permeability markers: FITC–dextran 4 kDa (FD4), FITC–dextran 10 kDa (FD10S) and [^{14}C]mannitol

Barrier integrity of the treated models was evaluated by co-administering the test drug with 1 µM [^{14}C]mannitol and either 75 µM FD4 or 30 µM FD10S to the donor side.

For EpiColon, cutoffs (C/O) for the transport of FD4, FD10S and [^{14}C]mannitol were newly established based on apparent permeability (P_{app}) data collected on days 8, 12, and 14 of differentiation. The reproducibility of [^{14}C]mannitol permeation across colon microtissues was assessed using three independent batches. Microtissue integrity was deemed acceptable when the P_{app} of the dosed drug met the predefined C/O criteria for co-dosed FD4 and [^{14}C]mannitol or FD10S and [^{14}C]mannitol. The TEER thresholds, as detailed in Section 2.3.4.1, were also confirmed.

For the Caco-2 monolayers, only wells that maintained TEER values ≥ 50% of their starting value by the end of the transport experiment, along with a [^{14}C]mannitol P_{app} of ≤ 3.0 x 10^{-6} cm/s, were included in the study (Kourula et al., 2023). FD4 or FD10S were similarly co-dosed with [^{14}C]mannitol, with a C/O threshold of ≤ 2.0 x 10^{-6} cm/s established using a similar approach.

2.3.5. Liquid chromatography–tandem mass spectrometry (LC–MS/MS) analysis

Samples obtained from transport studies involving EpiColon microtissues and Caco-2 monolayers were analyzed using LC–MS/MS to quantify selected analytes. Sample preparation involved protein precipitation using acetonitrile containing tolbutamide as an internal standard. Calibration solutions were prepared through serial dilutions in blank DMSO. Calibration standard samples were prepared by spiking blank matrix with the calibration solutions. The same volume of blank DMSO was added to the study samples. Both calibration solutions and study samples were processed concurrently. All samples were vortexed and centrifuged at 5000-6000 x g for 10 min. After centrifugation, the supernatant was injected into the liquid chromatography (LC) system for analysis.

2.3.6. Liquid chromatography (LC) optimization

Chromatographic separation from matrix interferences was achieved using a Nexera Ultra High-Performance Liquid Chromatography (UHPLC) system (Shimadzu) equipped with a reversed-phase UHPLC column (Waters).

Given substantial differences in the physicochemical properties of the analytes, a single combined LC method proved unfeasible. LC conditions were optimized to ensure efficient separation, sufficient retention of each analyte, and the required lower limit of quantification (LLOQ). Finalized LC conditions, optimized to combine the quantification of the selected analytes, are detailed in *Supplementary Table 3* (**Appendix B.1**, **Table S3**).

For chromatographic separation, extracted samples were injected onto the reversed-phase UHPLC column (**Table S3**) operated at 50 °C, using the UHPLC system (Shimadzu). Separation was carried out via gradient elution, starting with 85% aqueous mobile phase (mobile phase A) and gradually increasing the percentage of organic solvent (mobile phase B).

2.3.7. Mass spectrometry (MS) optimization

Mass spectrometric detection of all analytes was conducted using a Triple Quadrupole 6500+ instrument (Sciex, Framingham, USA) operated in either positive or negative ion mode, depending on the analyte. MS was operated in the positive ion mode using the TurboIonSpray™ interface (electrospray ionization) for budesonide, ketoprofen, ximelagatran, inogatran, sumatriptan, ranitidine, antipyrine, sulfasalazine, erythromycin, and cyclosporin A. Conversely, celecoxib, sulindac, and mesalazine were analyzed in negative ion mode. Fragmentation parameters were fine-tuned for each analyte's quantification, including tolbutamide, which served as a general internal standard. All MS parameters are comprehensively listed in *Supplementary Table 4* (**Appendix B.1**, **Table S4**).

2.3.8. Sample analysis

A log-log transposed linear regression model was used and peak area ratios of the analyte to its internal standard were plotted against the analyte concentrations. Sample concentrations were calculated by interpolation from the standard curves. The linearity of the instrument's response was validated through the back-calculated concentrations of the calibration samples, with calibration standard accuracies falling within 25% accuracy, and 30% accuracy at the LLOQ.

2.3.9. Reverse transcription-quantitative polymerase chain reaction (RT-qPCR): gene expression

RNA isolation from colon microtissues on day 11 of differentiation was performed at MatTek Corporation using the RNeasy Plus Mini Kit (Qiagen, #74134), following the manufacturer's protocol. The expression levels of 40 genes encoding specific human drug transporters were evaluated by RT-qPCR, utilizing RT^2 SYBR® Green qPCR Mastermix (Qiagen, #330503) and RT^2 Profiler™ PCR Array Kit (Qiagen, #330231), adhering to the manufacturer's instructions. Primer sequences for the genes analyzed can be retrieved via the corresponding *GenBank* accession numbers listed in *Supplementary Table 5* (**Appendix B.2**, **Table S5**).

2.4. Compound selection

As outlined in *Supplementary Table 2* (**Appendix B.1**, **Table S2**), the permeability of EpiColon was determined for 20 model drugs across 26 test conditions and compared with Caco-2. We first focused on 17 passively transported drugs, along with erythromycin in the presence of the P-gp inhibitor elacridar, as presented in Section 3.3. Following this, we selected two transporter substrates, which were discussed in Section 3.4.

The selection criteria included compounds routinely utilized as high and low permeability markers in standard in-house permeability assays, such as [^{3}H]metoprolol (high permeability in Caco-2, transcellular transport) and [^{3}H]atenolol (low permeability in Caco-2, predominantly paracellular transport)

Additionally, the selection encompassed colon-targeted drugs (e.g., budesonide and mesalazine); compounds exhibiting differential absorption between the small intestine and colon (e.g., sumatriptan); high passive permeability compounds (e.g., ketoprofen and budesonide); low passive permeability compounds (e.g., FITC–dextrans); and low permeability, transcellularly-transported compounds (e.g., erythromycin). Specific consideration was given to compounds that are substrates for P-gp, exemplified by [^{3}H]digoxin, and MRP2 and BCRP, represented by sulfasalazine.

Overall, priority was given to compounds with known intracolonic fraction absorbed (i.e. f_{abs}), including budesonide, ketoprofen, [^{3}H]metoprolol, [^{3}H]digoxin, ximelagatran, [^{3}H]atenolol, [^{14}C]cimetidine, sumatriptan and ranitidine. The focus extended to low permeability compounds, which fall within a similar permeability range when tested in Caco-2 monolayers, making it challenging to rank them accurately based on their P_{app} values.

2.5. Data analysis

Data analysis was performed using Microsoft® Excel (Redmond, WA, USA) and results were visualized using GraphPad Prism 10.1.2 software (San Diego, CA, USA).

2.5.1. Apparent permeability coefficient (P_{app})

Transport across colon microtissues or Caco-2 monolayers is expressed as a flux (dpm/s or µg/s). P_{app} was calculated from the slope of the transport time profile, divided by the surface area of the insert (0.6 cm^2 for EpiColon and 0.7 cm^2 for Caco-2 monolayers) and the initial measured concentration in the donor compartment. P_{app} for each compound was determined using Eq. (1):

$$\boldsymbol{P_{app}} = \frac{\mathbf{1}}{\boldsymbol{A \times C_{t0}}} + \frac{\boldsymbol{V_R \times \Delta C_R}}{\boldsymbol{\Delta t}} \quad (1)$$

, where P_{app} is the permeability coefficient (x10^{-6} cm/s) in either the apical-to-basolateral (AP→BL) or in basolateral-to-apical (BL→AP) direction; A is the area of the filter (cm^2); C_{t0} is the concentration of the respective starting solution (dpm/mL or ng/mL); V_R is the volume of the receiver compartment (mL); and $\Delta C_R/\Delta t$ represents the change in substance concentration over time in the receiver compartment (dpm/mL or ng/mL x s). The transport rate was derived from the linear portion of the test (or reference) compound concentration versus time curve in the receiver compartment.

2.5.2. Percent recovery

Percent recovery of compound, representing the remaining amount of compound in the compartments at the end of experiment, was calculated using Eq. (2):

$$\%\boldsymbol{recovery} = \frac{\boldsymbol{C_R \times V_R + C_D \times V_D}}{\boldsymbol{C_{t0} \times V_D}} \quad (2)$$

, where C_R is the concentration in the receiver compartment at the end of the experiment; C_D is the concentration in the donor compartment at end of experiment; C_{t0} is the initial concentration in the donor compartment; and V_R and V_D are the volumes of the receiver and donor compartments, respectively. Three recovery thresholds (>30%, >50%, and >80%) were compared between microtissues and Caco-2 monolayers.

2.5.3. Efflux ratio (ER)

Efflux ratio (ER), determined from bidirectional studies with digoxin and sulfasalazine, was calculated as the ratio between the secretory permeability, P_{app} [BL→AP], and the absorptive permeability, P_{app} [AP→BL], according to Eq. (3):

$$\boldsymbol{ER} = \frac{\boldsymbol{P_{app\,[BL \rightarrow AP]}}}{\boldsymbol{P_{app\,[AP \rightarrow BL]}}} \quad (3)$$

ER ≥ 2 suggests that the test drug is a substrate for an efflux transporter (Ayehunie et al., 2018).

2.5.4. In vitro-in vivo correlations (IVIVCs)

IVIVCs between the reported human fraction absorbed (f_{abs}) and log P_{app} [AP-BL] were established for EpiColon and Caco-2 using 17 passive diffusion drugs. To evaluate the relationship between log P_{app} and f_{abs} rankings, Spearman's rank correlation coefficient (r_s), a nonparametric measure ranging from -1 to +1, was employed, given the assumption of non-normally distributed data. Correlations strengths were categorized as follows: 0.00–0.19 (very weak), 0.20–0.39 (weak), 0.40–0.59 (moderate), 0.60–0.79 (strong), and 0.80–1.0 (very strong). All correlations were tested for statistical significance.

2.6. Statistical analysis

Statistical analyses were conducted using GraphPad Prism 10.1.2 software (San Diego, CA, USA). Data are presented as mean ± standard deviation (SD). To compare two groups, a two-tailed Mann–Whitney nonparametric test (*U*-test) was applied when appropriate. To assess statistical differences between more than two groups, an ordinary two-way ANOVA with Tukey's post hoc test for multiple comparisons was used for normally distributed data. For non-normally distributed data, the Kruskal-Wallis nonparametric test (*H*-test) was applied, followed by Dunn's multiple comparisons test. The significance level (α) was set at 0.05, with a 95% confidence interval (CI). Statistical significance was evaluated based on *p*-value, *P* (*ns* – not significant, *$P \leq 0.05$, **$P \leq 0.01$, ***$P \leq 0.001$, ****$P \leq 0.0001$). Asterisks (*) indicate significant differences. Specific statistical tests used to infer differences between groups, along with the number of tissue batches and technical replicates, are outlined in the corresponding figures or tables. For correlation analyses not covered in Section 2.5.4, Spearman's rank correlation coefficient (r_s) or the coefficient of determination (R^2) are provided as noted in the figures or tables, with all correlations tested for statistical significance.

3. Results and discussion

3.1. EpiColon demonstrates physiological barrier function and mirrors phenotypic, structural and cellular features of the human colon

Primary human colon epithelial cells were seeded onto single-well cell culture inserts under submerged conditions, followed by ALI culture. This approach resulted in the reconstruction of EpiColon tissues with differentiated tissue structure and morphology (**Fig. 1*a***).

In this study, we obtained differentiated colonic microtissues with average TEER values of 287.4 ± 55.44 Ω x cm^2 on day 13 (**Fig. 1*b***; *n* = 24) and 211.3 ± 80.23 Ω x cm^2 on day 14 (**Fig. S1*c$_3$***; *n* = 24) across two separate batches. These values fall within the physiological range observed for the human colon *in vivo* (Srinivasan et al., 2015). EpiColon demonstrated TEER ~1.8 times higher than that reported for its small intestine counterpart, EpiIntestinal™ (152.5 ± 39.00 Ω x cm^2) (Ayehunie et al., 2018; Markus et al., 2021), reflecting the inherently tighter mucosal barrier of the colon compared to the SI.

Comparable TEER values (~400 Ω x cm^2) were reported for isolated human colon tissue grown in a microfluidic platform (PREDICT96) over 14 days (Marr et al., 2023). Similarly, other studies have demonstrated average TEER values of 400 Ω x cm^2 for human rectal and ileal-derived monolayers (VanDussen et al., 2015). Notably, we observed a decrease in TEER from day 13 onward (**Fig. S1*c$_2$***), consistent with trends reported for one donor at day 11 in Marr et al.'s study (2023). This reduction in TEER was accompanied by a significant decline in total protein levels from day 11 to 25 (**Fig. S1*b***; ****$P \leq 0.0001$), suggesting optimal culture endpoints between days 11 and 14 of differentiation. Time-course TEER evaluations across three different batches (**Fig. S1*c$_{1–3}$***) revealed consistent profiles, irrespective of the tissue batch.

Paracellular transport in the intestinal epithelium is regulated by tight junctions (TJs) between epithelial cells (Horowitz et al., 2023; Monaco et al., 2021). A "tight" epithelium exhibits an equivalent low paracellular permeability (Monaco et al., 2021). The reported TEER values for *ex vivo* human SI tissues range from 12 to 120 Ω x cm^2, while those for *ex vivo* human colon tissues are between 300 and 400 Ω x cm^2. TEER values for Caco-2 monolayer cultures show considerable variability, largely due to factors such

as passage number and subclone heterogeneity, ranging from 195 to 2400 Ω x cm^2 (Darling et al., 2020; Hubatsch et al., 2007; Srinivasan et al., 2015). This variability extends beyond immortalized cell lines and is also observed in human organoid-derived monolayers, with TEER values from SI organoid monolayers sometimes exceeding those from the colon, a contrast to findings from human Ussing chamber studies (Parente et al., 2024). For instance, Kourula et al. reported TEER values of 1500 to 2000 Ω x cm^2 for human duodenal enteroid-derived monolayers (Kourula et al., 2023). However, such values can vary widely in the literature, spanning from 350 to 2000 Ω x cm^2, with Wright and colleagues reporting values as low as 350 Ω x cm^2 for human ileal-derived monolayers (Wright et al., 2023). These discrepancies highlight the substantial gap between epithelial barriers created *in vitro* and those observed *ex vivo*, especially when relying on TEER measurements.

The tested Caco-2 cell line displayed a TEER of 390.3 ± 25.42 Ω x cm^2. These Caco-2 monolayers exhibited significantly tighter paracellular junctions than EpiColon microtissues (****$P \leq 0.0001$), as shown in **Fig. S2**, which compares the mean TEER values at the culture endpoints for two batches of microtissues and Caco-2 monolayers. This finding may suggest an enhanced paracellular permeability of EpiColon compared to Caco-2, owing to less restrictive tight junctions (Monaco et al., 2021), a hypothesis supported by functional data. Although Caco-2 exhibited higher TEER values than EpiColon, these results align with those reported for *ex vivo* human colon tissues.

Histological (H&E staining) and immunohistochemical evaluation of the EpiColon microtissues at day 11 (**Fig. 1*c***, left panel) versus human colon samples (**Fig. 1*c***, right panel) revealed an *in vivo*-like tissue architecture. This included a multilayered structure comprising a basal cell layer positive for PanCK (epithelial marker) and Vimentin (mesenchymal marker), corresponding to a fibroblast-like population, with overlying epithelial cell layers also positive for PanCK, identifying the absorptive colonocytes. Alcian Blue staining indicated mucus production and the presence of goblet cells. Upon differentiation, microtissues lost their proliferative cells (Ki-67-positive cells), with only minimal proliferating colonic stem cells detected. These phenotypic and structural characteristics were consistent across different batches (**Fig. S1*a***). Collectively, these findings indicate that EpiColon exhibits partial differentiation, with limited cell polarization.

Most tissues exhibited a multilayered, stratified epithelium, interspersed with regions of simple cuboidal cells, rather than a fully mature simple columnar appearance, suggesting potential for further maturation. The absence of other cytokeratins, such as Cytokeratin 20 (CK20) (data not shown), corroborates this observation. The basal layer displayed a hybrid epithelial-mesenchymal phenotype, indicative of epithelial-mesenchymal transition (EMT), a critical developmental process whereby epithelial cells acquire mesenchymal, fibroblast-like characteristics (Marconi et al., 2021).

3.2. EpiColon provides enhanced dynamic range and resolution in distinguishing high molecular weight sugars compared to Caco-2

Fluorescent dextrans are commonly used to investigate paracellular transport across the intestinal epithelium (Emeh et al., 2024; Gleeson et al., 2024); therefore, to assess barrier integrity and paracellular permeability, [^{14}C]mannitol was co-dosed with either FD4 or FD10S, complementing TEER measurements.

We observed strong linear correlations between P_{app} [^{14}C]mannitol and P_{app} FD4 (**Fig. S3*a*$_1$**; R^2 = 0.88, ****$P \leq 0.0001$) and P_{app} [^{14}C]mannitol and P_{app} FD10S (**Fig. S3*b*$_1$**; R^2 = 0.75, ****$P \leq 0.0001$). These correlations were significantly stronger in EpiColon compared to Caco-2 monolayers for both FD4 (**Fig. S3*a*$_2$**; R^2 = 0.71, **P = 0.004) and FD10S (**Fig. S3*b*$_2$**; R^2 = 0.66, **P = 0.007). This underscores the utility of co-dosing [^{14}C]mannitol and a FITC–dextran as a reliable QC for microtissue integrity (**Fig. S3**).

Model-specific C/O thresholds were established for FD4, FD10S, and [^{14}C]mannitol (**Fig. 2*a***): $P_{app} \leq 3.5$ for FD4 (**Fig. 2*a*$_1$**), $P_{app} \leq 2.0$ for FD10S (**Fig. 2*a*$_2$**), and $P_{app} \leq 7.5$ for [^{14}C]mannitol (**Fig. 2*a*$_3$**), all expressed in x10^{-6} cm/s. Microtissue integrity was considered acceptable when the P_{app} met the C/O criteria for either FD4 and [^{14}C]mannitol or FD10S and [^{14}C]mannitol, and only microtissues showing TEER ≥ 100 Ω x cm^2 were used for transport studies.

When these thresholds were applied, the P_{app} distributions for FD4, FD10S, and [^{14}C]mannitol in EpiColon were compared to those in Caco-2 (**Fig. 2*b***). Interestingly, the violin plots demonstrated that EpiColon effectively distinguishes between two sugars with different molecular weights (**Fig. 2*b*$_1$** and **2*b*$_2$**), which are confined to the same permeability range in Caco-2. In line with FD4 and FD10S, EpiColon displayed higher paracellular permeability for [^{14}C]mannitol than Caco-2 (**Fig. 2*b*$_3$**), reflecting mannitol's primary transport through tight junctions via the paracellular pathway (Horowitz et al., 2023). All leakage markers ranked within the same permeability interval in Caco-2 (**Fig. 2*b***, light blue), reflecting the significantly tighter paracellular junctions (**Fig. S2**) that likely contribute to the underestimation of paracellular permeability.

Our data showed mean P_{app} values in EpiColon of 1.80 ± 0.54 for FD4, 0.96 ± 0.36 for FD10S, and 5.34 ± 1.21 for [^{14}C]mannitol (x10^{-6} cm/s). For Caco-2 monolayers in our study, P_{app} for all leakage markers (including [^{14}C]mannitol) ranged between 0.14 and 0.67 (x10^{-6} cm/s).

For FD4, Miyake and colleagues reported a P_{app} of 2.5 x 10^{-6} cm/s in isolated human ileum tissue in a mini-Ussing chamber (Miyake et al., 2013), while Eslami Amirabadi *et al*. determined a P_{app} of ∼1 × 10^{-6} cm/s in a human colonic explant Chip model (Eslami Amirabadi et al., 2022). Comparatively, FD4 permeability in Caco-2 monolayers is typically reported as < 8 × 10^{-8} cm/s (Gleeson et al., 2024).

Overall, the FD4 data obtained from EpiColon were higher compared to those of Caco-2 but in line with native colonic tissue, likely due to the tighter junctions in Caco-2. These findings suggest that EpiColon has greater physiological relevance to *in vivo* conditions compared to conventional Caco-2 monolayers.

Fig. 2*c*$_1$ (based on P_{app}) and **Fig. 2*c*$_2$** (based on % to the start) compare endpoint permeability for FITC–dextrans in EpiColon microtissues (day 14) and Caco-2. EpiColon showed a higher dynamic range and resolution, enabling differentiation between FD4 and FD10S (**Fig. 2*c*$_1$** and **2*c*$_2$**; FD4 *vs*. FD10S, **$P \leq 0.01$), while Caco-2 cells were unable to distinguish between them (**Fig. 2*c*$_1$** and **2*c*$_2$**; FD4 *vs*. FD10S, $P > 0.05$, *ns*). Noteworthy, EpiColon exhibited significantly enhanced paracellular permeability for both FD4 and FD10S compared to Caco-2 (****$P \leq 0.0001$).

Further comparisons of FITC–dextrans at days 8 and 12 from a single batch of tissues (**Fig. S4**) revealed substantial maturation of EpiColon, with reductions in paracellular permeability of approximately 10-fold for FD4 and 20-fold for FD10S. By day 12, EpiColon already provided a clear distinction between FD4 and FD10S (**Fig. S4*a*$_2$**, ****$P \leq 0.0001$; **Fig S4*b*$_2$**, **$P \leq 0.01$), which was not observed at day 8 (**Fig. S4*a*$_1$** and **Fig S4*b*$_1$**, $P > 0.05$, *ns*).

The reproducibility of an *in vitro* method is essential for its utility (Ayehunie et al., 2018). To assess the reproducibility of colon microtissue integrity, [^{14}C]mannitol permeation was used as a control, and results were compared across three batches (**Fig. S5**). Violin plots for [^{14}C]mannitol showed consistent P_{app} distributions across batches after C/O implementation (**Fig. S5*b***; **Table S6**).

The QC for EpiColon relies on evaluating its permeability using FD4 and [^{14}C]mannitol or FD10S and [^{14}C]mannitol. Unlike Caco-2 cells (data not shown for [^{14}C]mannitol), no significant relationship was observed between the P_{app} of FD4, FD10S, or [^{14}C]mannitol and TEER (**Fig. S6**). This is a limitation since TEER is a non-invasive method that can be easily employed to quantify barrier integrity before drug testing (Srinivasan et al., 2015). Although some non-radioactive fluorophores are sometimes reported to lack the sensitivity required to detect subtle changes in monolayer permeability (Duffy and Murphy, 2001), due to low specific activity or fluorophore instability, co-dosing with a radiolabeled marker offers a high-sensitivity control for assessing microtissue integrity.

3.3. *EpiColon exhibits faster P_{app} in the low permeability range for both paracellular and transcellular pathways*

SI microtissues offer advantages over other systems like 3D intestinal organoids, primarily due to their ready-to-use format, lower variability, and enhanced polarization (Ayehunie et al., 2018; Markus et al., 2021). With distinct apical (AP) and basolateral (BP) surfaces, these tissues facilitate permeability assessments in both the absorptive (AP→BL, mimicking luminal-to-bloodstream permeation) and secretory (BL→AP, emulating bloodstream-to-lumen transport) directions. Similarly, EpiColon tissue is also ready-to-use, with clearly defined AP and BL surfaces, making it well-suited for direct permeability measurements. A schematic diagram of EpiColon is displayed in **Fig. 1*a***.

It is important to note that the P_{app} represents the permeability of a cell monolayer to a given compound (Esaki et al., 2024). Thus, P_{app} values for the same compound may vary depending on the model utilized. Herein, we compared the permeability of two intestinal barrier systems: EpiColon microtissues and Caco-2 monolayers, using a panel of 17 drugs selected according to criteria outlined in Section 2.4.

Fig. 3 presents the P_{app} in the absorptive direction, P_{app} [AP-BL], for the 17 model drugs, categorized into high permeability (**Fig. 3*a***; upper panel, n = 6) and low permeability (**Fig. 3*b***; lower panel, n = 11). Barrier integrity was monitored using TEER measurements conducted before ($TEER_{pre\text{-}assay}$) and after ($TEER_{post\text{-}assay}$) each transport experiment (**Fig. S1*d***), alongside FITC–dextran/[^{14}C]mannitol transport (P_{app}). The absence of significant differences between pre- and post-assay TEER values confirmed the stability of the barrier integrity within the microtissues throughout the assays (**Fig. S1*d***; $P > 0.05$, *ns*).

While both EpiColon and Caco-2 models effectively discriminated between high and low-permeability compounds, they show discernible trends in their permeability profiles.

Caco-2 monolayers generally exhibited higher P_{app} values in the high permeability range (**Fig. 3*a***; Caco-2 > EpiColon). Conversely, EpiColon demonstrated faster P_{app} in the low permeability space for both paracellular (e.g., [^{3}H]atenolol and FD4, denoted by red arrows) and transcellular pathways (e.g., erythromycin in the presence of the P-gp inhibitor elacridar, marked with a red arrow with white stripes) (**Fig. 3*b***; EpiColon > Caco-2). These findings support previous observations, showing that EpiColon offers better resolution in the low permeability range [0.96 for FD10S to 5.83 for sumatriptan] compared to Caco-

2 [0.14 for FD10S to 2.66 for ranitidine] (x10^{-6} cm/s). The enhanced paracellular permeability observed in EpiColon may be attributed to the physiological "looseness" (Takenaka et al., 2014) of its tight junctions.

Recovery thresholds (>30%, >50%, and >80%) were analyzed, and the categorization of drugs in both models was found to be comparable, with 76.9% of compounds demonstrating a recovery of >80% in both systems (**Table S7**). Detailed recovery data for each drug in EpiColon and Caco-2 monolayers are provided in **Fig. S7**. Compounds that consistently exhibited poor recovery in both models (e.g., celecoxib and cyclosporin A, known to accumulate within cell monolayers; data not shown) were excluded from further analysis.

Additionally, the multilayered structure of EpiColon must be considered. We hypothesize that the mesenchymal basal cell layer may offer an additional site for drug accumulation, potentially hindering the flux of lipophilic compounds. This may result in an underestimation of the P_{app} for BCS Class II drugs, potentially explaining the discrepancy observed for ketoprofen in **Fig. 3*a***. Further investigations are warranted to elucidate the impact of this basal layer on drug transport.

3.4. EpiColon reveals functional activity for major efflux transporters

The bioavailability of orally administered drugs is vastly influenced by the activity of drug transporters. Among these, the ATP-binding cassette (ABC) efflux transporters, specifically multidrug resistance protein 1 (MDR1, P-glycoprotein, P-gp), MRP2 and BCRP, are highly expressed on the apical (luminal) membrane of enterocytes. These transporters play a crucial role in limiting the absorption of numerous clinically important drugs by actively effluxing them back into the intestinal lumen (Englund et al., 2006; Estudante et al., 2013). Notably, MRP2 is of particular interest due to its unique apical localization (as opposed to MRP1–5, which are located basolaterally), protecting the organism from toxic substances while also modulating the absorption of certain drugs (Lu et al., 2022).

To investigate the functional activity of these transporters in EpiColon microtissues, we conducted bidirectional transport studies using [^{3}H]digoxin (a P-gp substrate) and sulfasalazine (a MRP2/BCRP substrate) and compared the results with those obtained from Caco-2 monolayers (**Fig. 4**). Permeability experiments were performed to measure P_{app} [AP→BL] and P_{app} [BL→AP] (**Fig. 4*a*$_1$–*b*$_2$**), and the efflux ratios (ERs) were calculated (**Fig. 4*c*$_1$** and **4*c*$_2$**).

In both systems, the absorptive transport of [^{3}H]digoxin and sulfasalazine was lower than the secretory transport, resulting in ER ≥ 2.0, which confirms active transport from the basolateral to the apical side (**Fig. 4*c*$_1$** and **4*c*$_2$**). ERs in EpiColon were 2.32-fold for MDR1 and 3.34-fold for MRP2/BCRP (**Fig. 4*c*$_1$**; **Table S8**), notably lower than those observed in Caco-2 cells, where MDR1 exhibited an ER of 17.6-fold and MRP2/BCRP 72.0-fold (**Fig. 4*c*$_2$**; **Table S9**). Since sulfasalazine is recognized as a substrate for BCRP, which mediates its efflux alongside MRP2 (Dahan and Amidon, 2010; Estudante et al., 2013), careful interpretation of results is warranted, as the contribution of BCRP was not elucidated in our study. However, based on a preliminary bidirectional transport study using EpiColon, in which estrone-3-sulfate was employed as a BCRP substrate and an efflux ratio of less than 2 was observed (data not shown), we hypothesize that the observed efflux of sulfasalazine in EpiColon may be mostly attributed to MRP2.

Comparative studies have previously highlighted higher efflux ratios for digoxin in Caco-2 cells than in more complex models like duodenal enteroid-derived monolayers (Kourula et al., 2023). Our results align

with these observations, demonstrating similar transport activities and lower ERs for the P-gp substrate [^{3}H]digoxin in EpiColon relative to Caco-2 and enteroid-derived models. Mols et al. (2005) examined the transport of sulfasalazine across Caco-2 monolayers and rat ileal-derived Ussing chambers, reporting a P_{app} [AP→BL] of 0.21 ± 0.02 x 10^{-6} cm/s and a P_{app} [BL→AP] of 2.97 ± 0.02 x 10^{-6} cm/s in Caco-2, yielding an ER of 14 (Mols et al., 2005), approximately 5.1-fold lower than our findings. Additionally, Dahan and Amidon (2010) noted an ER of 30 in Caco-2 cells (around 2.4-fold lower than observed in our study), which was reduced to 4 in the presence of indomethacin, suggesting that BCRP-mediated efflux remained active (Dahan and Amidon, 2010). This highlights substantial variability in the literature and suggests that efflux-mediated transport may be artificially elevated in Caco-2 cells.

Furthermore, RT-qPCR analysis confirmed the expression of *ABCB1*/MDR-1 in EpiColon microtissues (**Table S5**), aligning with our drug transport experiments. Out of 40 evaluated genes, several relevant transporters, including *ABCC3*/MRP3 (a key transporter in the colon) (Drozdzik et al., 2019), *SLC16A1*/MCT1 (enriched at the protein and mRNA levels in the colon) (Drozdzik et al., 2019), *SLCO2B1*/OATP2B1, and *SLC15A1*/PEPT1 were also expressed. *SLCO1B3*/OATP1B3, primarily expressed in the liver and not detectable in the intestine (Drozdzik et al., 2019), served as a negative control. Altogether, EpiColon microtissues exhibited functional barrier properties and active efflux by P-gp and MRP2/BCRP.

3.5. EpiColon may be suitable to rank order small molecules within the low permeability category

There is a growing demand for useful and reproducible *in vitro* colonic models to predict human drug absorption accurately. Such models are essential, particularly those that yield results comparable to *in vivo* data (Apostolou et al., 2021; Marr et al., 2023; Mitrofanova et al., 2024; Rozehnal et al., 2012; Sato et al., 2011).

For the compounds tested in this study, a significant correlation (**Fig. S8**; R^2 = 0.62, n = 9, *P = 0.0118) was observed between the reported human intracolonic fraction absorbed (i.c. f_{abs}) and the human per oral administration fraction absorbed (p.o. f_{abs}). Notable outliers in this relationship, such as sumatriptan (i.c. f_{abs} of 15% and p.o. f_{abs} of 78%) and ranitidine (i.c. f_{abs} of 9% and p.o. f_{abs} of 65%), underscore the necessity for more colonic-like models.

We established IVIVCs between reported human f_{abs} and log P_{app} [AP-BL] for both EpiColon and Caco-2, utilizing 17 model drugs (**Fig. 5**).

Preference was given to compounds with known i.c. f_{abs}; when unavailable, p.o. f_{abs} was used. Only the passive absorptive permeability (P_{app} [AP-BL]) was included in the analysis (reflecting passively transported drugs or those in the presence of an inhibitor). Celecoxib and cyclosporin A were excluded due to poor recovery (**Fig. S7**). **Table 1** provides a summary of the physicochemical properties, f_{abs}, and absorptive apparent permeability (P_{app} [AP-BL]) for the tested drugs.

Various statistical correlation methods can substantiate the relationship between datasets, such as Pearson's product-moment correlation coefficient for normally distributed data and Spearman's rank correlation coefficient (r_s) for non-normally distributed data (Niven and Deutsch, 2012). Notably, r_s does not assume a linear relationship between variables; rather, it assesses how effectively an arbitrary monotonic function can describe the relationship of rankings between two variables, without presuming

a specific frequency distribution or normality (Niven and Deutsch, 2012). Additionally, r_s is generally more robust against outliers compared to Pearson's coefficient (Niven and Deutsch, 2012). Therefore, r_s was employed to evaluate the relationships between the rankings of human f_{abs} and log P_{app} [AP-BL].

A significant, strong positive correlation between reported human f_{abs} and the logarithmically transformed P_{app} [AP-BL] values was identified for both EpiColon (**Fig. 5*a*$_1$**; r_s = 0.68, n = 17, $^{**}P$ = 0.004) and Caco-2 (**Fig. 5*b*$_1$**; r_s = 0.68, n = 17, $^{**}P$ = 0.003). Interestingly, the Spearman's rank correlation coefficient (r_s) was identical for both models, despite some discrepancies in rank order. It is noteworthy that the Caco-2 cells employed in this study were maintained at a low passage interval (19–23), which may elucidate these findings.

Ayehunie et al. previously reported similar correlations between human f_{abs} and log P_{app}, noting that the ileal microtissue EpiIntestinal™ demonstrated a stronger correlation with human absorption data (R^2 = 0.91, n = 11) compared to Caco-2 cells (R^2 = 0.71, n = 11) (Ayehunie et al., 2018). This enhanced predictive capacity was attributed to EpiIntestinal™'s structural and functional characteristics, such as its barrier integrity and transporter expression, which more closely mimic the human ileum.

In contrast, even though EpiColon successfully replicates several structural, cellular and functional characteristics of the human colon – such as the presence of both epithelial and mesenchymal cells, mucus production (absent in Caco-2), physiological barrier function (TEER values that reflect native colonic barrier properties), and the expression of key efflux transporters (MDR1 and MRP2/BCRP, with lower efflux ratios than Caco-2) – these attributes did not result in a stronger correlation with human absorption data compared to Caco-2 cells.

Historical data supports strong IVIVCs primarily for compounds with high permeability (Pham-The et al., 2013). Thus, we categorized our dataset into high permeability (**Fig. 5**, middle panel, n = 6) and low permeability (**Fig. 5**, lower panel, n = 11) groups, based on the Biopharmaceutics Classification System (BCS) (**Table 1**).

For high permeability compounds, EpiColon demonstrated a moderate positive correlation and with a higher r_s (**Fig. 5*a*$_2$**; r_s = 0.58, n = 6, P > 0.05, *ns*) compared to Caco-2 (**Fig. 5*b*$_2$**; r_s = 0.23, n = 6, P > 0.05, *ns*), which exhibited a weak correlation, and in general the rank-order relationships were maintained with some disconnects (e.g., ketoprofen). The mesenchymal layer in EpiColon may contribute to an underestimation of P_{app} for BCS Class II drugs, potentially explaining this disconnect.

For the low permeability subset, both models showed weaker correlations: EpiColon revealed a weak positive correlation (**Fig. 5*a*$_3$**; r_s = 0.29, n = 11, P > 0.05, *ns*), while Caco-2 displayed a very weak negative correlation (**Fig. 5*b*$_3$**; r_s = -0.059, n = 11, P > 0.05, *ns*). All r_s values for the various group comparisons are compiled in **Table S10**. Ranitidine is highlighted in the lower panel due to its disconnect in rank order relationships within the low permeability group.

While EpiColon showed higher r_s values for both high and low permeability groups compared to Caco-2, caution is warranted in interpretation, as these correlations were not statistically significant. Nevertheless, the findings for the low permeability group are consistent with previous observations, suggesting that EpiColon may be suitable for ranking compounds within the low permeability space – a limitation often observed with conventional models such as Caco-2 or MDCK cell monolayers. These traditional models typically fail to accurately estimate paracellular transport contributions due to their tighter monolayer structure compared to the GI epithelium (Ayehunie et al., 2018; Costa and Ahluwalia,

2019; Huth et al., 2021; Lemmens et al., 2021). In addition to the enhancement of paracellular transport observed in EpiColon, a similar trend was noted for the transcellular pathway, as evidenced by the increased passive permeability of erythromycin compared to Caco-2 cells (**Fig. 3*b***). The wider P_{app} window observed in EpiColon microtissues within the low permeability range may provide an advantage for rank-ordering small molecules relative to conventional models.

4. Conclusion

This study introduces EpiColon, a novel human organotypic 3D colon microtissue, and explores its potential as a platform for investigating colonic drug disposition, with an emphasis on permeability ranking.

EpiColon mimics the human colonic epithelium, exhibiting differentiation characterized by the presence of both epithelial and mesenchymal fibroblast-like cells, goblet cells, and mucus production. It demonstrates TEER comparable to native colonic tissues and shows functional activity of pivotal efflux transporters, such as MDR1 and MRP2/BCRP, with lower efflux ratios than Caco-2 cells. By enhancing both paracellular and transcellular transport pathways for low permeability drugs, EpiColon emerges as a valuable preclinical tool for evaluating drug disposition and ranking compounds within this category.

Despite these strengths, EpiColon has certain limitations. The presence of a multilayered stratified epithelium, consisting of flat to some cuboidal cells, suggests that further epithelial maturation could be achieved. Moreover, the current prototype's low throughput restricts its scalability for high-volume screenings, though a high throughput version is under development by MatTek Corporation. It is also important to acknowledge that EpiColon microtissues are still simplified models of the human colon. The use of descending colon tissue—characterized by lower absorption capacity compared to the proximal colon due to reduced water content and consequently less dissolved compound—along with the absence of immune cells, vasculature, microbiota component, and mechanical cues or flow, may impact its replicative accuracy and its utility for certain research applications.

In summary, EpiColon represents a step forward in colonic drug disposition, offering a more physiologically relevant system with improved structural and functional attributes that complement the widely used Caco-2 model. Addressing its current limitations will be vital for broadening its applicability and impact across both academic research and the pharmaceutical industry. Moreover, EpiColon holds promise in reducing the reliance on extensive animal studies, thereby aligning with the principles of the 3Rs (replacement, reduction, and refinement).

Declaration of Generative AI and AI-assisted technologies in the writing process

During the preparation of this work the authors used Gen AI by Johnson and Johnson (GPT-3.5 Turbo model) in order to check spelling and grammar. After using this tool/service, the authors reviewed and edited the content as needed and take full responsibility for the content of the publication.

CRediT authorship contribution statement

Pedro G.M. Canhão: Writing – original draft, Writing – review & editing, Validation, Project administration, Conceptualization, Methodology, Data curation, Investigation, Formal analysis, Visualization. **Jan Snoeys:**

Writing – review & editing, Supervision, Conceptualization. **Suzy Geerinckx:** Methodology, Data curation, Investigation. **Marjolein van Heerden:** Data curation, Investigation. **An Van den Bergh:** Writing – review & editing, Project administration, Conceptualization. **Camden Holm:** Methodology, Data curation, Investigation. **Jan Markus:** Writing – review & editing, Conceptualization. **Seyoum Ayehunie:** Writing – review & editing, Resources, Conceptualization. **Mario Monshouwer:** Writing – review & editing, Resources. **Raymond Evers:** Writing – review & editing, Resources, Conceptualization. **Patrick Augustijns:** Writing – review & editing, Project administration, Supervision, Resources, Funding acquisition, Data curation, Conceptualization. **Stephanie Kourula:** Writing – review & editing, Project administration, Supervision, Resources, Funding acquisition, Data curation, Conceptualization.

Declaration of competing interest

Authors declare no conflicts of interest, financial or otherwise.

Data availability

Data supporting the conclusions of this article will be made available upon reasonable request.

Acknowledgements

This work was funded by the European Union's Horizon 2020 research and innovation program under the Marie Skłodowska-Curie grant agreement no. 956851 (COLOTAN). We thank Marjolein Crabbe and Jan Serroyen (Discovery Statistics, Johnson & Johnson Innovative Medicine, Belgium) for the insights and stimulating discussions on the statistical analysis of the in vitro-in vivo correlations.

Supplementary materials

Appendix A. Supplementary figures

Supplementary figures associated with this article can be found, in the online version, at [*insert DOI*].

Appendix B. Supplementary tables

Supplementary tables related to this article are available in the online version at [*insert DOI*].

References

Ambrosini, Y.M., Park, Y., Jergens, A.E., Shin, W., Min, S., Atherly, T., Borcherding, D.C., Jang, J., Allenspach, K., Mochel, J.P., Kim, H.J., 2020. Recapitulation of the accessible interface of biopsy-derived canine intestinal organoids to study epithelial-luminal interactions. PLoS One 15, 1–17. https://doi.org/10.1371/journal.pone.0231423

Apostolou, A., Panchakshari, R.A., Banerjee, A., Manatakis, D. V, Paraskevopoulou, M.D., 2021. A novel microphysiological colon platform to decipher mechanisms driving human intestinal permeability. Cell Mol Gastroenterol Hepatol 1–61. https://doi.org/10.1016/j.jcmgh.2021.07.004

Arian, C., Mahony, E.O., MacDonald, J.W., Bammler, T.K., Donowitz, M., Kelly, E.J., Thummel, K.E., 2024. Human Enteroid Monolayers: A Novel, Functionally-Stable Model for Investigating Oral Drug Disposition. Drug Metabolism and Disposition 52, 1–43. https://doi.org/10.1124/dmd.124.001551

Ayehunie, S., Landry, T., Stevens, Z., Armento, A., Hayden, P., Klausner, M., 2018. Human Primary Cell-Based Organotypic Microtissues for Modeling Small Intestinal Drug Absorption. Pharm Res 35, 1–18. https://doi.org/10.1007/s11095-018-2362-0

Costa, J., Ahluwalia, A., 2019. Advances and Current Challenges in Intestinal in vitro Model Engineering: A Digest. Front Bioeng Biotechnol 7, 1–14. https://doi.org/10.3389/fbioe.2019.00144

Cui, Y., Claus, S., Schnell, D., Runge, F., Maclean, C., 2020. In-Depth Characterization of EpiIntestinal Microtissue as a Model for Intestinal Drug Absorption and Metabolism in Human. Pharmaceutics 12, 1–15. https://doi.org/10.3390/pharmaceutics12050405

Dahan, A., Amidon, G.L., 2010. MRP2 mediated drug-drug interaction: Indomethacin increases sulfasalazine absorption in the small intestine, potentially decreasing its colonic targeting. Int J Pharm 386, 216–220. https://doi.org/10.1016/j.ijpharm.2009.11.021

Dahlgren, D., Roos, C., Sjögren, E., Lennernäs, H., 2015. Direct in Vivo Human Intestinal Permeability (P eff) Determined with Different Clinical Perfusion and Intubation Methods. J Pharm Sci 104, 2702–2726. https://doi.org/10.1002/jps.24258

d'Aldebert, E., Quaranta, M., Sébert, M., Bonnet, D., Kirzin, S., Portier, G., Duffas, J.P., Chabot, S., Lluel, P., Allart, S., Ferrand, A., Alric, L., Racaud-Sultan, C., Mas, E., Deraison, C., Vergnolle, N., 2020. Characterization of Human Colon Organoids From Inflammatory Bowel Disease Patients. Front Cell Dev Biol 8, 1–13. https://doi.org/10.3389/fcell.2020.00363

Darling, N.J., Mobbs, C.L., González-Hau, A.L., Freer, M., Przyborski, S., 2020. Bioengineering Novel in vitro Co-culture Models That Represent the Human Intestinal Mucosa With Improved Caco-2 Structure and Barrier Function. Front Bioeng Biotechnol 8, 1–15. https://doi.org/10.3389/fbioe.2020.00992

Di, L., Artursson, P., Avdeef, A., Benet, L.Z., Houston, J.B., Kansy, M., Kerns, E.H., Lennernäs, H., Smith, D.A., Sugano, K., 2020. The Critical Role of Passive Permeability in Designing Successful Drugs. ChemMedChem 15, 1862–1874. https://doi.org/10.1002/cmdc.202000419

Drozdzik, M., Busch, D., Lapczuk, J., Müller, J., Ostrowski, M., Kurzawski, M., Oswald, S., 2019. Protein Abundance of Clinically Relevant Drug Transporters in the Human Liver and Intestine: A Comparative Analysis in Paired Tissue Specimens. Clin Pharmacol Ther 105, 1204–1212. https://doi.org/10.1002/cpt.1301

Duffy, S.L., Murphy, J.T., 2001. Colorimetric Assay to Quantify Macromolecule Diffusion across Endothelial Monolayers. Biotechniques 31, 495–501. https://doi.org/10.2144/01313st02

Ehrhardt, C., Kim, K.-J., 2008. Drug Absorption Studies: In Situ, In Vitro and In Silico Models. Springer 77–86. https://doi.org/10.1007/978-0-387-74901-3

Emeh, P., Breitholtz, K., Berg, S., Vedin, C., Englund, M., Uggla, T., Antonsson, M., Nunes, F., Hilgendorf, C., Bergström, C.A.S., Davies, N., 2024. Experiences and Translatability of In Vitro and In Vivo Models to

Evaluate Caprate as a Permeation Enhancer. Mol Pharm 21, 313–324. https://doi.org/10.1021/acs.molpharmaceut.3c00872

Englund, G., Rorsman, F., Rönnblom, A., Karlbom, U., Lazorova, L., Gråsjö, J., Kindmark, A., Artursson, P., 2006. Regional levels of drug transporters along the human intestinal tract: Co-expression of ABC and SLC transporters and comparison with Caco-2 cells. European Journal of Pharmaceutical Sciences 29, 269–277. https://doi.org/10.1016/j.ejps.2006.04.010

Esaki, T., Yonezawa, T., Ikeda, K., 2024. A new workflow for the effective curation of membrane permeability data from open ADME information. J Cheminform 16, 1–11. https://doi.org/10.1186/s13321-024-00826-z

Eslami Amirabadi, H., Donkers, J.M., Wierenga, E., Ingenhut, B., Pieters, L., Stevens, L., Donkers, T., Westerhout, J., Masereeuw, R., Bobeldijk-Pastorova, I., Nooijen, I., Van De Steeg, E., 2022. Intestinal explant barrier chip: Long-term intestinal absorption screening in a novel microphysiological system using tissue explants. Lab Chip 22, 326–342. https://doi.org/10.1039/d1lc00669j

Estudante, M., Morais, J.G., Soveral, G., Benet, L.Z., 2013. Intestinal drug transporters: An overview. Adv Drug Deliv Rev 65, 1340–1356. https://doi.org/10.1016/j.addr.2012.09.042

Gleeson, J.P., Zhang, S.Y., Subelzu, N., Ling, J., Nissley, B., Ong, W., Nofsinger, R., Kesisoglou, F., 2024. Head-to-Head Comparison of Caco-2 Transwell and Gut-on-a-Chip Models for Assessing Oral Peptide Formulations. Mol Pharm 21, 1–9. https://doi.org/10.1021/acs.molpharmaceut.4c00210

Hammer, T., Langholz, E., 2020. The epidemiology of inflammatory bowel disease: balance between East and West? A narrative review. Dig Med Res 3, 48–48. https://doi.org/10.21037/dmr-20-149

Horowitz, A., Chanez-Paredes, S.D., Haest, X., Turner, J.R., 2023. Paracellular permeability and tight junction regulation in gut health and disease. Nat Rev Gastroenterol Hepatol 20, 417–432. https://doi.org/10.1038/s41575-023-00766-3

Hua, S., 2020. Advances in Oral Drug Delivery for Regional Targeting in the Gastrointestinal Tract - Influence of Physiological, Pathophysiological and Pharmaceutical Factors. Front Pharmacol 11, 1–22. https://doi.org/10.3389/fphar.2020.00524

Hubatsch, I., Ragnarsson, E.G.E., Artursson, P., 2007. Determination of drug permeability and prediction of drug absorption in Caco-2 monolayers. Nat Protoc 2, 2111–2119. https://doi.org/10.1038/nprot.2007.303

Huth, F., Domange, N., Poller, B., Vapurcuyan, A., Durrwell, A., Hanna, I.D., Faller, B., 2021. Predicting Oral Absorption for Compounds Outside the Rule of Five Property Space. J Pharm Sci 110, 2562–2569. https://doi.org/10.1016/j.xphs.2021.01.029

In, J.G., Foulke-Abel, J., Clarke, E., Kovbasnjuk, O., 2019. Human colonoid monolayers to study interactions between pathogens, commensals, and host intestinal epithelium. Journal of Visualized Experiments 2019, 1–11. https://doi.org/10.3791/59357

Kaplan, G.G., 2015. The global burden of IBD: From 2015 to 2025. Nat Rev Gastroenterol Hepatol 12, 720–727. https://doi.org/10.1038/nrgastro.2015.150

Kourula, S., Derksen, M., Jardi, F., Jonkers, S., van Heerden, M., Verboven, P., Theuns, V., Van Asten, S., Huybrechts, T., Kunze, A., Frazer-Mendelewska, E., Lai, K.W., Overmeer, R., Roos, J.L., Vries, R.G.J., Boj, S.F., Monshouwer, M., Pourfarzad, F., Snoeys, J., 2023. Intestinal organoids as an in vitro platform to characterize disposition, metabolism, and safety profile of small molecules. European Journal of Pharmaceutical Sciences 1–15. https://doi.org/10.1016/j.ejps.2023.106481

Koziolek, M., Augustijns, P., Berger, C., Cristofoletti, R., Dahlgren, D., Keemink, J., Matsson, P., McCartney, F., Metzger, M., Mezler, M., Niessen, J., Polli, J.E., Vertzoni, M., Weitschies, W., Dressman, J., 2023. Challenges in Permeability Assessment for Oral Drug Product Development. Pharmaceutics 15, 1–38. https://doi.org/10.3390/pharmaceutics15102397

Kraiczy, J., Nayak, K.M., Howell, K.J., Ross, A., Forbester, J., Salvestrini, C., Mustata, R., Perkins, S., Andersson-Rolf, A., Leenen, E., Liebert, A., Vallier, L., Rosenstiel, P.C., Stegle, O., Dougan, G., Heuschkel, R., Koo, B.K., Zilbauer, M., 2019. DNA methylation defines regional identity of human intestinal epithelial organoids and undergoes dynamic changes during development. Gut 68, 49–61. https://doi.org/10.1136/gutjnl-2017-314817

Kus, M., Ibragimow, I., Piotrowska-Kempisty, H., 2023. Caco-2 Cell Line Standardization with Pharmaceutical Requirements and In Vitro Model Suitability for Permeability Assays. Pharmaceutics 15, 1–15. https://doi.org/10.3390/pharmaceutics15112523

Kwon, O., Jung, K.B., Lee, K.R., Son, Y.S., Lee, H., Kim, J.J., Kim, K., Lee, S., Song, Y.K., Jung, J., Park, K., Kim, D.S., Son, M.J., Lee, M.O., Han, T.S., Cho, H.S., Oh, S.J., Chung, H., Kim, S.H., Chung, K.S., Kim, J., Jung, C.R., Son, M.Y., 2021. The development of a functional human small intestinal epithelium model for drug absorption. Sci Adv 7, 1–18. https://doi.org/10.1126/sciadv.abh1586

Larregieu, C.A., Benet, L.Z., 2014. Distinguishing between the permeability relationships with absorption and metabolism to improve BCS and BDDCS predictions in early drug discovery. Mol Pharm 11, 1335–1344. https://doi.org/10.1021/mp4007858

Larregieu, C.A., Benet, L.Z., 2013. Drug discovery and regulatory considerations for improving in silico and in vitro predictions that use caco-2 as a surrogate for human intestinal permeability measurements. AAPS Journal 15, 483–497. https://doi.org/10.1208/s12248-013-9456-8

Lemmens, G., Van Camp, A., Kourula, S., Vanuytsel, T., Augustijns, P., 2021. Drug disposition in the lower gastrointestinal tract: Targeting and monitoring. Pharmaceutics 13, 1–53. https://doi.org/10.3390/pharmaceutics13020161

Lu, R., Zhou, Y., Ma, J., Wang, Y., Miao, X., 2022. Strategies and Mechanism in Reversing Intestinal Drug Efflux in Oral Drug Delivery. Pharmaceutics 14, 1–20. https://doi.org/10.3390/pharmaceutics14061131

Macedo, M.H., Martínez, E., Barrias, C.C., Sarmento, B., 2020. Development of an Improved 3D in vitro Intestinal Model to Perform Permeability Studies of Paracellular Compounds. Front Bioeng Biotechnol 8, 1–17. https://doi.org/10.3389/fbioe.2020.524018

Madden, L.R., Nguyen, T. V., Garcia-Mojica, S., Shah, V., Le, A. V., Peier, A., Visconti, R., Parker, E.M., Presnell, S.C., Nguyen, D.G., Retting, K.N., 2018. Bioprinted 3D Primary Human Intestinal Tissues

Model Aspects of Native Physiology and ADME/Tox Functions. iScience 2, 156–167. https://doi.org/10.1016/j.isci.2018.03.015

Mahe, M.M., Sundaram, N., Watson, C.L., Shroyer, N.F., Helmrath, M.A., 2015. Establishment of human epithelial enteroids and colonoids from whole tissue and biopsy. Journal of Visualized Experiments 2015, 1–13. https://doi.org/10.3791/52483

Marcellinaro, R., Spoletini, D., Grieco, M., Avella, P., Cappuccio, M., Troiano, R., Lisi, G., Garbarino, G.M., Carlini, M., 2024. Colorectal Cancer: Current Updates and Future Perspectives. J Clin Med 13, 1–12. https://doi.org/10.3390/jcm13010040

Marconi, G.D., Fonticoli, L., Rajan, T.S., Pierdomenico, S.D., Trubiani, O., Pizzicannella, J., Diomede, F., 2021. Epithelial-Mesenchymal Transition (EMT): The Type-2 EMT in Wound Healing, Tissue Regeneration and Organ Fibrosis. Cells 10, 1–14. https://doi.org/10.3390/cells

Markus, J., Landry, T., Stevens, Z., Scott, H., Llanos, P., Debatis, M., Armento, A., Klausner, M., Ayehunie, S., 2021. Human small intestinal organotypic culture model for drug permeation, inflammation, and toxicity assays. In Vitro Cell Dev Biol Anim 57, 160–173. https://doi.org/10.1007/s11626-020-00526-6

Marr, E.E., Mulhern, T.J., Welch, M., Keegan, P., Caballero-Franco, C., Johnson, B.G., Kasaian, M., Azizgolshani, H., Petrie, T., Charest, J., Wiellette, E., 2023. A platform to reproducibly evaluate human colon permeability and damage. Sci Rep 13, 1–15. https://doi.org/10.1038/s41598-023-36020-8

Michiba, K., Maeda, K., Shimomura, O., Miyazaki, Y., Hashimoto, S., Oda, T., Kusuhara, H., 2022. Usefulness of Human Jejunal Spheroid-Derived Differentiated Intestinal Epithelial Cells for the Prediction of Intestinal Drug Absorption in Humans. Drug Metabolism and Disposition 50, 204–213. https://doi.org/10.1124/dmd.121.000796

Mitrofanova, O., Nikolaev, M., Xu, Q., Broguiere, N., Cubela, I., Camp, J.G., Bscheider, M., Lutolf, M.P., 2024. Bioengineered human colon organoids with in vivo-like cellular complexity and function. Cell Stem Cell 8, 1175–1186. https://doi.org/10.1016/j.stem.2024.05.007

Miyake, M., Toguchi, H., Nishibayashi, T., Higaki, K., Sugita, A., Koganei, K., Kamada, N., Kitazume, M.T., Hisamatsu, T., Sato, T., Okamoto, S., Kanai, T., Hibi, T., 2013. Establishment of Novel Prediction System of Intestinal Absorption in Humans Using Human Intestinal Tissues. J Pharm Sci 102, 2564–2571. https://doi.org/10.1002/jps.23609

Mols, R., Deferme, S., Augustijns, P., 2005. Sulfasalazine transport in in-vitro, ex-vivo and in-vivo absorption models: contribution of efflux carriers and their modulation by co-administration of synthetic nature-identical fruit extracts. Journal of Pharmacy and Pharmacology 57, 1565–1573. https://doi.org/10.1211/jpp.57.12.0006

Monaco, A., Ovryn, B., Axis, J., Amsler, K., 2021. The Epithelial Cell Leak Pathway. Int J Mol Sci 22, 1–26. https://doi.org/10.3390/ijms22147677

Müller, J., Keiser, M., Drozdzik, M., Oswald, S., 2017. Expression, regulation and function of intestinal drug transporters: an update. Biol Chem 398, 175–192. https://doi.org/10.1515/hsz-2016-0259

Niven, E.B., Deutsch, C. V., 2012. Calculating a robust correlation coefficient and quantifying its uncertainty. Comput Geosci 40, 1–9. https://doi.org/10.1016/j.cageo.2011.06.021

Ölander, M., Wiśniewski, J.R., Matsson, P., Lundquist, P., Artursson, P., 2016. The Proteome of Filter-Grown Caco-2 Cells with a Focus on Proteins Involved in Drug Disposition. J Pharm Sci 105, 817–827. https://doi.org/10.1016/j.xphs.2015.10.030

Panaccione, R., Ferraz, J.G., Beck, P., 2005. Advances in medical therapy of inflammatory bowel disease. Curr Opin Pharmacol 5, 566–572. https://doi.org/10.1016/j.coph.2005.08.003

Parente, I.A., Chiara, L., Bertoni, S., 2024. Exploring the potential of human intestinal organoids: Applications, challenges, and future directions. Life Sci 352, 1–14. https://doi.org/10.1016/j.lfs.2024.122875

Peña, M.A., 2022. Solubilization and Controlled Release Strategy of Poorly Water-Soluble Drugs. Pharmaceuticals 15, 1–3. https://doi.org/10.3390/ph15111353

Peters, M.F., Landry, T., Pin, C., Maratea, K., Dick, C., Wagoner, M.P., Choy, A.L., Barthlow, H., Snow, D., Stevens, Z., Armento, A., Scott, C.W., Ayehunie, S., 2019. Human 3D Gastrointestinal Microtissue Barrier Function As a Predictor of Drug-Induced Diarrhea. Toxicological Sciences 168, 3–17. https://doi.org/10.1093/toxsci/kfy268

Pham-The, H., González-Álvarez, I., Bermejo, M., Garrigues, T., Le-Thi-Thu, H., Cabrera-Pérez, M.Á., 2013. The Use of Rule-Based and QSPR Approaches in ADME Profiling: A Case Study on Caco-2 Permeability. Mol Inform 32, 459–479. https://doi.org/https://doi.org/10.1002/minf.201200166

Pretorius, E., Bouic, P.J.D., 2009. Permeation of four oral drugs through human intestinal mucosa. AAPS PharmSciTech 10, 270–275. https://doi.org/10.1208/s12249-009-9207-4

Roos, C., Dahlgren, D., Sjögren, E., Tannergren, C., Abrahamsson, B., Lennernäs, H., 2017. Regional Intestinal Permeability in Rats: A Comparison of Methods. Mol Pharm 14, 4252–4261. https://doi.org/10.1021/acs.molpharmaceut.7b00279

Rozehnal, V., Nakai, D., Hoepner, U., Fischer, T., Kamiyama, E., Takahashi, M., Yasuda, S., Mueller, J., 2012. Human small intestinal and colonic tissue mounted in the Ussing chamber as a tool for characterizing the intestinal absorption of drugs. European Journal of Pharmaceutical Sciences 46, 367–373. https://doi.org/10.1016/j.ejps.2012.02.025

Sato, T., Stange, D.E., Ferrante, M., Vries, R.G.J., Van Es, J.H., Van Den Brink, S., Van Houdt, W.J., Pronk, A., Van Gorp, J., Siersema, P.D., Clevers, H., 2011. Long-term expansion of epithelial organoids from human colon, adenoma, adenocarcinoma, and Barrett's epithelium. Gastroenterology 141, 1762–1772. https://doi.org/10.1053/j.gastro.2011.07.050

Sato, T., Vries, R.G., Snippert, H.J., Van De Wetering, M., Barker, N., Stange, D.E., Van Es, J.H., Abo, A., Kujala, P., Peters, P.J., Clevers, H., 2009. Single Lgr5 stem cells build crypt-villus structures in vitro without a mesenchymal niche. Nature 459, 262–265. https://doi.org/10.1038/nature07935

Sjöberg, Å., Lutz, M., Tannergren, C., Wingolf, C., Borde, A., Ungell, A.L., 2013. Comprehensive study on regional human intestinal permeability and prediction of fraction absorbed of drugs using the Ussing

chamber technique. European Journal of Pharmaceutical Sciences 48, 166–180. https://doi.org/10.1016/j.ejps.2012.10.007

Srinivasan, B., Kolli, A.R., Esch, M.B., Abaci, H.E., Shuler, M.L., Hickman, J.J., 2015. TEER Measurement Techniques for In Vitro Barrier Model Systems. J Lab Autom 20, 107–126. https://doi.org/10.1177/2211068214561025

Steigert, S., Brouwers, J., Verbeke, K., Vanuytsel, T., Augustijns, P., 2024. Characterization of luminal contents from the fasted human proximal colon. European Journal of Pharmaceutical Sciences 200, 1–8. https://doi.org/10.1016/j.ejps.2024.106821

Streekstra, E.J., Kiss, M., van den Heuvel, J., Nicolaï, J., van den Broek, P., Botden, S.M.B.I., Stommel, M.W.J., van Rijssel, L., Ungell, A.L., van de Steeg, E., Russel, F.G.M., de Wildt, S.N., 2022. A proof of concept using the Ussing chamber methodology to study pediatric intestinal drug transport and age-dependent differences in absorption. Clin Transl Sci 15, 2392–2402. https://doi.org/10.1111/cts.13368

Takenaka, T., Harada, N., Kuze, J., Chiba, M., Iwao, T., Matsunaga, T., 2014. Human small intestinal epithelial cells differentiated from adult intestinal stem cells as a novel system for predicting oral drug absorption in humans. Drug Metabolism and Disposition 42, 1947–1954. https://doi.org/10.1124/dmd.114.059493

Tannergren, C., Bergendal, A., Lennernäs, H., Abrahamsson, B., 2009. Toward an increased understanding of the barriers to colonic drug absorption in humans: implications for early controlled release candidate assessment. Mol Pharm 6, 60–73. https://doi.org/10.1021/mp800261a

van der Hee, B., Madsen, O., Vervoort, J., Smidt, H., Wells, J.M., 2020. Congruence of Transcription Programs in Adult Stem Cell-Derived Jejunum Organoids and Original Tissue During Long-Term Culture. Front Cell Dev Biol 8, 1–13. https://doi.org/10.3389/fcell.2020.00375

VanDussen, K.L., Marinshaw, J.M., Shaikh, N., Miyoshi, H., Moon, C., Tarr, P.I., Ciorba, M.A., Stappenbeck, T.S., 2015. Development of an enhanced human gastrointestinal epithelial culture system to facilitate patient-based assays. Gut 64, 911–920. https://doi.org/10.1136/gutjnl-2013-306651

Vinarov, Z., Abdallah, M., Agundez, J.A.G., Allegaert, K., Basit, A.W., Braeckmans, M., Ceulemans, J., Corsetti, M., Griffin, B.T., Grimm, M., Keszthelyi, D., Koziolek, M., Madla, C.M., Matthys, C., McCoubrey, L.E., Mitra, A., Reppas, C., Stappaerts, J., Steenackers, N., Trevaskis, N.L., Vanuytsel, T., Vertzoni, M., Weitschies, W., Wilson, C., Augustijns, P., 2021. Impact of gastrointestinal tract variability on oral drug absorption and pharmacokinetics: An UNGAP review. European Journal of Pharmaceutical Sciences 162, 1–33. https://doi.org/10.1016/j.ejps.2021.105812

Wang, Y., Chiang, I.L., Ohara, T.E., Fujii, S., Cheng, J., Muegge, B.D., Ver Heul, A., Han, N.D., Lu, Q., Xiong, S., Chen, F., Lai, C.W., Janova, H., Wu, R., Whitehurst, C.E., VanDussen, K.L., Liu, T.C., Gordon, J.I., Sibley, L.D., Stappenbeck, T.S., 2019. Long-Term Culture Captures Injury-Repair Cycles of Colonic Stem Cells. Cell 179, 1144-1159.e15. https://doi.org/10.1016/j.cell.2019.10.015

Wright, C.W., Li, N., Shaffer, L., Hill, A., Boyer, N., Alves, S.E., Venkataraman, S., Biswas, K., Lieberman, L.A., Mohammadi, S., 2023. Establishment of a 96-well transwell system using primary human gut

organoids to capture multiple quantitative pathway readouts. Sci Rep 13, 1–12. https://doi.org/10.1038/s41598-023-43656-z

Xu, G., Xu, Y., Zheng, T., Liu, T., 2024. Type 2 diabetes and inflammatory bowel disease: a bidirectional two-sample Mendelian randomization study. Sci Rep 14, 1–9. https://doi.org/10.1038/s41598-024-55869-x

Yoshida, S., Honjo, T., Iino, K., Ishibe, R., Leo, S., Shimada, T., Watanabe, T., Ishikawa, M., Maeda, K., Kusuhara, H., Shiraki, N., Kume, S., 2021. Generation of Human-Induced Pluripotent Stem Cell-Derived Functional Enterocyte-Like Cells for Pharmacokinetic Studies. Stem Cell Reports 16, 295–308. https://doi.org/10.1016/j.stemcr.2020.12.017

Zachos, N.C., Kovbasnjuk, O., Foulke-Abel, J., In, J., Blutt, S.E., De Jonge, H.R., Estes, M.K., Donowitz, M., 2016. Human enteroids/colonoids and intestinal organoids functionally recapitulate normal intestinal physiology and pathophysiology. Journal of Biological Chemistry 291, 3759–3766. https://doi.org/10.1074/jbc.R114.635995

Zietek, T., Giesbertz, P., Ewers, M., Reichart, F., Weinmüller, M., Urbauer, E., Haller, D., Demir, I.E., Ceyhan, G.O., Kessler, H., Rath, E., 2020. Organoids to Study Intestinal Nutrient Transport, Drug Uptake and Metabolism – Update to the Human Model and Expansion of Applications. Front Bioeng Biotechnol 8, 1–14. https://doi.org/10.3389/fbioe.2020.577656

■ Main Figures (Figs. 1–5)

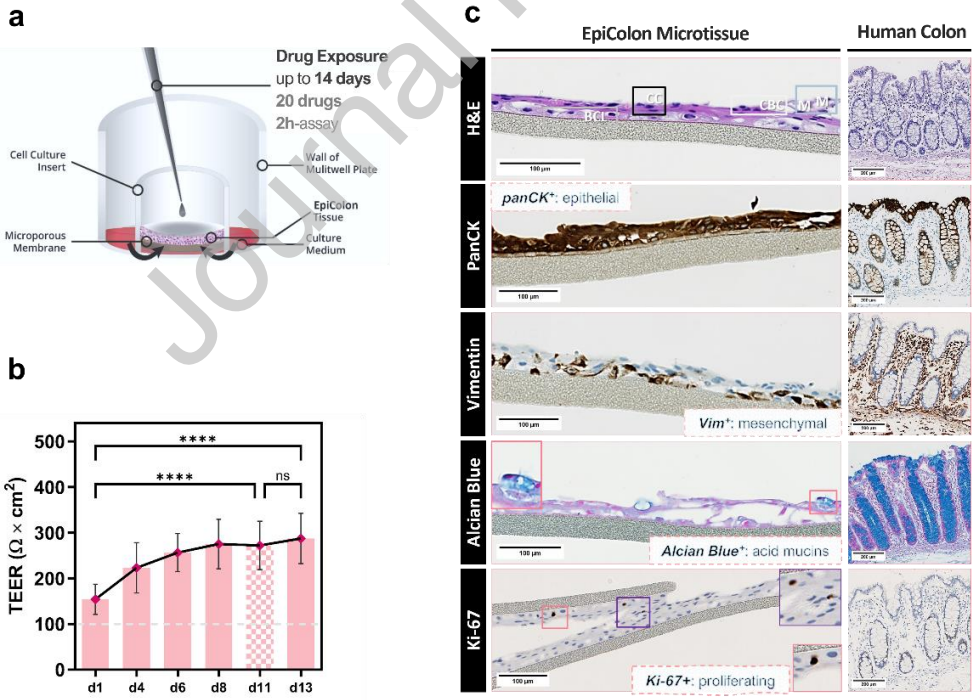

Fig. 1. EpiColon demonstrates physiological barrier function and mirrors structural and cellular features of the human colon. (a) Schematic of the human 3D colon microtissue model. Structural and functional evaluations of EpiColon tissues were conducted using 20 benchmark compounds following a differentiation period of up to 14 days. The schematic was adapted with permission from MatTek Corporation. **(b) TEER evaluation over time** (d1 to d13; pale pink bars). Error bars are mean ± SD from one batch of microtissues, with resistance values recorded on days 1, 4, 6, 8, 11 and 13 (n = 18–48). The complete profile for this batch is shown in **Fig. S1*c*$_2$**. Statistical differences were assessed using the Kruskal-Wallis test, followed by Dunn's multiple comparisons test (*ns* – not significant, ****$P \leq 0.0001$). Pink dotted bars (day 11) indicate the days on which drug transport assays were conducted. The grey dashed line at 100 Ω x cm² marks the intactness threshold; tissues with TEER values below this were excluded from functional evaluations. **(c) Histology and immunohistochemistry analysis.** EpiColon microtissue (*left panels*) compared to healthy human colon tissue (*right panels*) immunostained for (*from top to bottom*): Hematoxylin and Eosin (H&E), Pan-Cytokeratin (PanCK), Vimentin, Alcian Blue and Marker of Proliferation Kiel 67 (Ki-67). Data are representative images from one batch at day 11 of differentiation. Insets display high magnification images of the corresponding highlighted pink or purple areas. Abbreviations (*upper left panel*): BCL, basal cell layer; CBC, simple cuboidal epithelial cells; CC, simple columnar epithelial cells; and M, mucus-like structures. Scale bars: *left panels* (EpiColon microtissue) in black, 100 µm; *right panels* (human colon tissue) in dark grey, 200 µm.

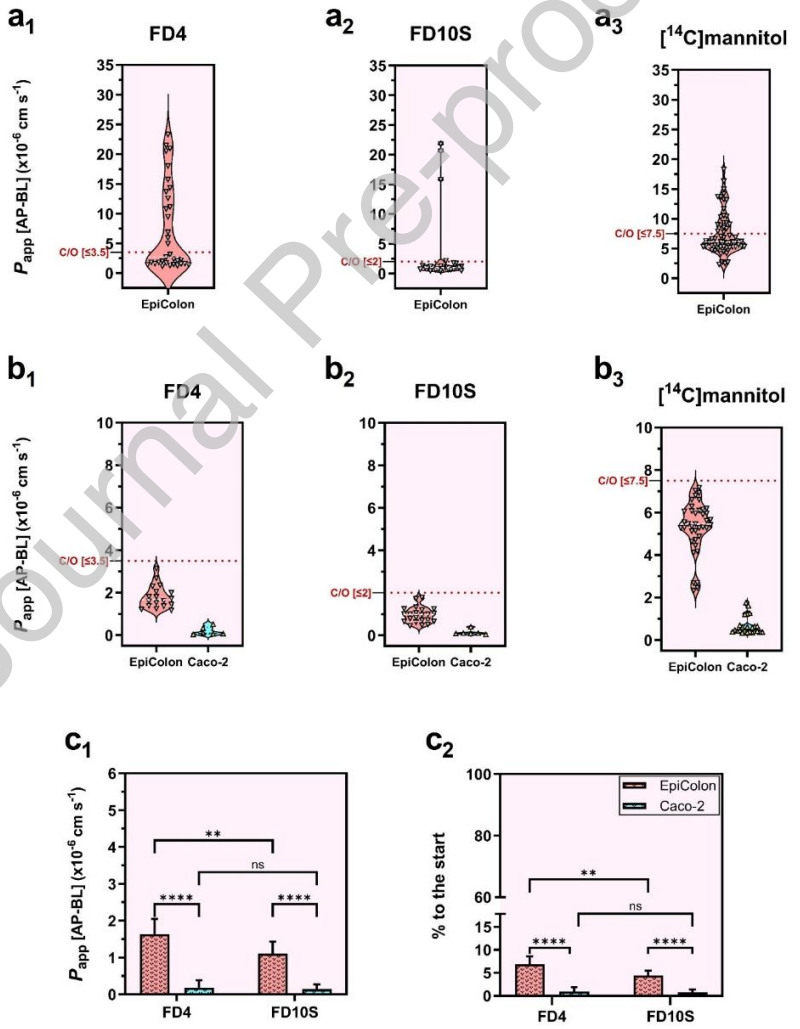

Fig. 2. EpiColon provides enhanced dynamic range and resolution in distinguishing high molecular weight sugars compared to Caco-2. (a) Quality control and cutoff (C/O) establishment for EpiColon. Violin plots illustrate the apparent permeability (P_{app}) distributions (pink) for **(a_1)** FITC-dextran 4 kDa (FD4; *n* = 33), **(a_2)** FITC-dextran 10 kDa (FD10S; *n* = 26), and **(a_3)** [^{14}C]mannitol (*n* = 60). C/O thresholds, indicated by red dotted lines, were determined from P_{app} data collected on days 8, 12, and 14 of differentiation using a single batch of EpiColon tissues. Thresholds were set where the data began to level off: ≤3.5 for FD4, ≤2.0 for FD10S, and ≤7.5 for [^{14}C]mannitol. Grey dotted lines mark the 25th and 75th percentiles, while white dashed lines indicate the median. Grey upside-down triangles represent individual P_{app} values (x10^{-6} cm/s). **(b) Comparison of leakage markers between EpiColon and Caco-2 after C/O implementation.** Violin plots depict the P_{app} distribution for **(b_1)** FD4 (EpiColon: *n* = 18; Caco-2: *n* = 6), **(b_2)** FD10S (EpiColon: *n* = 22; Caco-2: *n* = 6), and **(b_3)** [^{14}C]mannitol (EpiColon: *n* = 39; Caco-2: *n* = 24) following the exclusion of non-intact tissues based on predefined C/O values. Pink distributions represent EpiColon, while light blue denotes Caco-2. Grey dotted lines show the 25th and 75th percentiles, and white dashed lines represent the median. Each triangle indicates an individual P_{app} value (grey fill, upside-down for EpiColon; yellow fill for Caco-2) (x10^{-6} cm/s). **(c) Endpoint assessment of EpiColon and Caco-2 permeability for FITC-dextrans. (c_1)** (*Lower left panel*) Mean P_{app} [AP-BL] values and **(c_2)** (*lower right panel*) % to the start for EpiColon (red) and Caco-2 (blue) for FD4 and FD10S. EpiColon data are presented as mean ± SD from one batch of tissues assessed on day 14 of differentiation. Analyses for days 8 and 12 are shown in in **Fig.S4**. Statistical significance was determined using an ordinary two-way ANOVA analysis with Tukey's *post hoc* test for multiple comparisons (*ns* – not significant, ***P* ≤ 0.01, *****P* ≤ 0.0001).

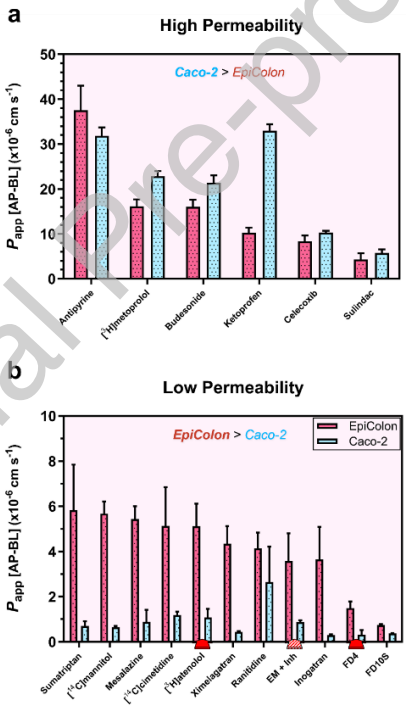

Fig. 3. EpiColon exhibits faster P_{app} in the low permeability range for both paracellular and transcellular pathways. **(a)** P_{app} [AP-BL] values of EpiColon (red bars) and Caco-2 (light blue bars) are shown for high permeability compounds (*upper panel*, *n* = 6): antipyrine, [^{3}H]metoprolol, budesonide, ketoprofen, celecoxib and sulindac; and **(b)** low permeability drugs (*lower panel*, *n* = 11): sumatriptan, [^{14}C]mannitol, mesalazine, [^{14}C]cimetidine, [^{3}H]atenolol, ximelagatran, ranitidine, erythromycin (EM) + Inhibitor (Inh), inogatran, FITC-dextran 4 kDa (FD4) and FITC-dextran 10 kDa (FD10S). Data represent mean values ± SD from at least duplicate wells within a single batch of tissues cultured to the endpoint. In the lower panel, red upper arrows highlight [^{3}H]atenolol and FD4 as examples of enhanced paracellular transport in EpiColon, while "EM + Inh", marked by a red upper arrow with white stripes, exemplifies enhanced transcellular transport. "Inh" refers to the P-gp inhibitor elacridar (GF120918) at 5 µM.

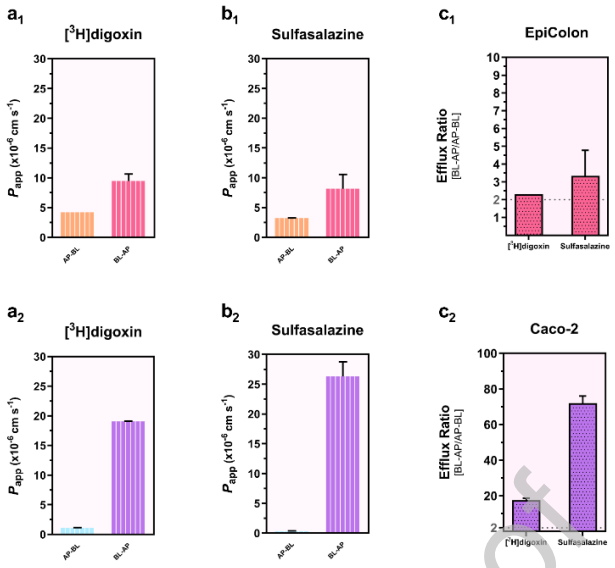

Fig. 4. EpiColon reveals functional activity for major efflux transporters. Activity of MDR1/P-gp ([^{3}H]digoxin), as well as MRP2 and BCRP (sulfasalazine), based on bidirectional permeability assays with EpiColon and Caco-2 monolayers. (a$_1$-b$_2$) Apparent permeability from apical-to-basolateral (P_{app} [AP-BL]; absorptive) and basolateral-to-apical (P_{app} [BL-AP]; secretory) compartments in EpiColon (**a$_1$,b$_1$**, *upper panel*; orange and red bars) and Caco-2 (**a$_2$,b$_2$**, *lower panel*; light and dark blue bars) following exposure to: **(a$_1$,a$_2$)** [^{3}H]digoxin (1 µM) and **(b$_1$,b$_2$)** sulfasalazine (EpiColon: 10 µM; Caco-2: 1 µM) over a 2-hour incubation period. **(c)** Comparison of efflux ratios (P_{app} [BL-AP] / P_{app} [AP-BL]) for [^{3}H]digoxin and sulfasalazine across EpiColon (**c$_1$**, *upper right corner*; red bars) and Caco-2 (**c$_2$**, *lower right corner*; dark blue bars). Drugs with an efflux ratio ≥ 2, denoted by the dotted grey line, are classified as substrates of efflux transporters. Error bars represent mean ± S.D. from at least one experiment. P_{app} values and efflux ratios for EpiColon and Caco-2 are provided in **Tables S8** and **S9**, respectively.

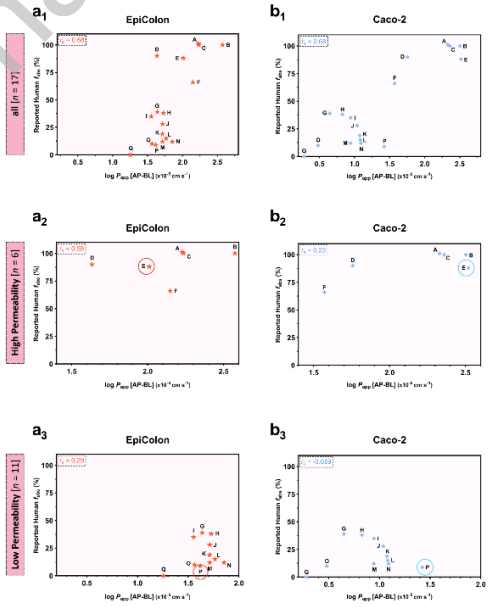

Fig. 5. EpiColon may help rank order small molecules in the low permeability category. ***In vitro-in vivo*** **correlations (IVIVCs) between the reported human fraction absorbed (f_{abs}) and log P_{app} [AP-BL] for 17 benchmark drugs tested in EpiColon and Caco-2.** **(a_1-a_3)** Correlations in EpiColon (*left panels*, red stars) and **(b_1-b_3)** Caco-2 monolayers (*right panels*, light blue rhombuses) are shown for: **(a_1,b_1)** all evaluated drugs (A to Q; *n* = 17), with Spearman's rank correlation coefficients (r_s) of 0.68 (***P* = 0.004) for EpiColon and 0.68 (***P* = 0.003) for Caco-2; **(a_2,b_2)** high permeability (A to F; *n* = 6) with r_s of 0.58 for EpiColon and 0.23 for Caco-2; and **(a_3,b_3)** low permeability (G to Q; *n* = 11), with r_s of 0.29 for EpiColon and -0.059 for Caco-2. Spearman's rank correlation coefficients (r_s) indicate the statistical dependence between the rankings of f_{abs} and log P_{app} and are displayed on the respective plots. Compound IDs are as follows: A, Budesonide; B, Antipyrine; C, [^{3}H]metoprolol; D, Sulindac; E, Ketoprofen; F, [^{3}H]digoxin + GF120918; G, Ximelagatran; H, [^{14}C]mannitol; I, Erythromycin + GF120918; J, [^{3}H]atenolol; K, [^{14}C]cimetidine; L, Sumatriptan; M, Mesalazine; N, Sulfasalazine + MK571; O, Inogatran; P, Ranitidine; and Q, FITC-dextran 4 kDa (FD4). Disconnects in rank-order relationships are highlighted with red and blue circles for Ketoprofen (E) and Ranitidine (P). P_{app} data are derived from at least one batch of tissues, with a minimum of 2 wells per compound (*n* = 2–24). P_{app} values for EpiColon and Caco-2, along with f_{abs} for the listed drugs, are compiled in **Table 1**. Correlation analyses and interpretations are summarized in **Table S10**.

■ Main Tables (Table 1)

■ **Table 1. Physicochemical properties, fraction absorbed (f_{abs}) and passive apparent permeability (P_{app} [AP→BL]) for a panel of 17 compounds in EpiColon and Caco-2.** Letters (A to Q) denote each compound used in the correlation analysis. Cyclosporin A and celecoxib were excluded due to consistently low recovery metrics across both models.

ID	Compound	BCS class	Permeability class	EpiColon P_{app} [AP→BL]^{a,*} (x10^{-6} cm/s)	Caco-2 P_{app} [AP→BL]^{b,*} (x10^{-6} cm/s)	Reported Human i.c. f_{abs}^{c} (%)	Reported Human p.o. f_{abs}^{d} (%)
A	Budesonide	I	High	**16.9** ± 0.88 (3)	**21.3** ± 1.71 (3)	101	100
B	Antipyrine	I	High	**37.5** ± 5.47 (3)	**31.8** ± 1.87 (3)		100
C	[^{3}H]metoprolol	I	High	**17.3** ± 1.54 (6)	**22.9** ± 1.16 (3)	100	95
D	Sulindac	II	High	**4.31** ± 1.38 (3)	**5.72** ± 0.87 (3)		90
E	Ketoprofen	II	High	**10.3** ± 1.14 (2)	**33.0** ± 1.41 (3)	88	100
F	[^{3}H]digoxin + GF120918	I	High	**14.1** ± 1.69 (2)	**3.72** ± 0.16 (3)	66	81
G	Ximelagatran	III	Low	**4.35** ± 0.79 (3)	**0.44** ± 0.03 (3)	39	45
H	[^{14}C]mannitol	III	Low	**5.34** ± 1.21 (39)	**0.67** ± 0.42 (24)		38
I	Erythromycin + GF120918	IV	Low	**3.57** ± 1.24 (2)	**0.88** ± 0.07 (2)		35
J	[^{3}H]atenolol	III	Low	**5.31** ± 0.85 (5)	**1.09** ± 0.37 (3)	28	56
K	[^{14}C]cimetidine	III	Low	**5.15** ± 1.71 (3)	**1.19** ± 0.15 (3)	19	64
L	Sumatriptan	III	Low	**5.83** ± 2.01 (3)	**1.21** ± 0.25 (3)	15	78
M	Mesalazine	IV	Low	**5.16** ± 0.38 (3)	**0.88** ± 0.53 (2)		12
N	Sulfasalazine + MK571	IV	Low	**7.15** ± 5.55 (3)	**1.23** ± 0.02 (3)		12
O	Inogatran	III	Low	**3.65** ± 1.44 (2)	**0.30** ± 0.03 (3)		10
P	Ranitidine	III	Low	**4.15** ± 0.69 (2)	**2.66** ± 1.56 (3)	9	65

Q	FD4	*n.a.*	Zero	**1.80** ± 0.54 (18)	**0.19** ± 0.19 (6)	0

[a-b] P_{app} values are reported as the mean ± S.D. ($n = x$) from at least one experiment, with a minimum of 2 wells per compound. x represents the number of replicates.

[c] **Human fraction absorbed f_{abs} i.c.** data were sourced from **Elezović *et al.* (2021)**, **Fredlund *et al.* (2017)**, **Sjöberg *et al.* (2013)** and **Tannergren *et al.* (2009).** Intracolonic fractions were used when available, except for antipyrine, sulindac, [^{14}C]mannitol, erythromycin + GF120918, mesalazine, sulfasalazine + MK571, inogatran, and FD4, for which p.o. fractions were employed.

[d] **Human fraction absorbed f_{abs} p.o.** data were obtained from **Fredlund *et al.* (2017)**, **Huth *et al.* (2021)**, **Larregieu and Benet (2014)**, **Sjöberg *et al.* (2013)**, **Tannergren *et al.* (2009)**, **Tannergren *et al.* (2023)** and **Yamashita *et al.* (2000).**

***** Abbreviations in square brackets symbolize the direction of the transport experiment. **AP→BL** denotes apical-to-basolateral (absorptive). Only absorptive permeability, **P_{app} [AP→BL]**, was used for correlation analyses. *n.a.* indicates non applicable.